

# Morphing Quantum Codes

Michael Vasmer<sup>1,2,\*</sup> and Aleksander Kubica<sup>1,2,3,4</sup>

<sup>1</sup>*Perimeter Institute for Theoretical Physics, Waterloo, Ontario N2L 2Y5, Canada*

<sup>2</sup>*Institute for Quantum Computing, University of Waterloo, Waterloo, Ontario N2L 3G1, Canada*

<sup>3</sup>*AWS Center for Quantum Computing, Pasadena, California 91125, USA*

<sup>4</sup>*California Institute of Technology, Pasadena, California 91125, USA*



(Received 29 December 2021; accepted 13 July 2022; published 8 August 2022)

We introduce a morphing procedure that can be used to generate new quantum codes from existing quantum codes. In particular, we morph the 15-qubit Reed-Muller code to obtain a  $[[10,1,2]]$  code that is the smallest-known stabilizer code with a fault-tolerant logical  $T$  gate. In addition, we construct a family of hybrid color-toric codes by morphing the color code. Our code family inherits the fault-tolerant gates of the original color code, implemented via constant-depth local unitaries. As a special case of this construction, we obtain toric codes with fault-tolerant multiqubit control- $Z$  gates. We also provide an efficient decoding algorithm for hybrid color-toric codes in two dimensions and numerically benchmark its performance for phase-flip noise. We expect that morphing may also be a useful technique for modifying other code families such as triorthogonal codes.

DOI: [10.1103/PRXQuantum.3.030319](https://doi.org/10.1103/PRXQuantum.3.030319)

## I. INTRODUCTION

The techniques of quantum error correction seem to be indispensable in the quest to build a large-scale quantum computer. Not only do we need to protect fragile qubits from environmental noise but we also need to perform quantum circuits fault tolerantly. The celebrated threshold theorem [1–3] proves that scalable fault-tolerant quantum computation is possible in principle and, moreover, that fault tolerance can be achieved with constant overhead for particular families of quantum error-correcting codes [4,5]. However, this is not the end of the story, as these asymptotic results can hide large constant factors and the requirements of quantum error correction [6–10] are still beyond the capabilities of today’s hardware [11–15]. Therefore, it is imperative to develop new quantum codes that are more efficient, more resilient to noise, and more tailored to hardware.

We introduce a theoretical tool for modifying quantum codes, called morphing, that allows us to systematically construct new codes from existing codes. Morphing does not change the number of logical qubits encoded into a code; however, it changes other properties of a code,

including the number of physical qubits, and it may also change the code distance, the stabilizer weights, and the implementation of logical gates. Consequently, morphing enables us to trade off different code parameters against each other in order to satisfy the constraints of a particular hardware platform, e.g., the number of physical qubits can be decreased at the cost of complicating the implementation of some logical gates.

We apply morphing to the 15-qubit Reed-Muller code, thereby constructing a  $[[10,1,2]]$  code with a fault-tolerant  $T$  gate. To our knowledge, this is the smallest-known stabilizer code with a fault-tolerant implementation of this gate. We investigate the performance of the  $[[10,1,2]]$  code in magic state distillation (MSD), finding that it may lead to advantages over previous MSD protocols based on small codes [16,17]. Our  $[[10,1,2]]$  protocol is the first example of an MSD protocol mixing different input magic states and we expect that our approach may be used to improve other MSD protocols.

By morphing the color code [18–20], we construct a family of hybrid color-toric (HCT) codes, which inherit the fault-tolerant logical gates of the color code. Starting from an initial color code, we can construct HCT codes with different stabilizer weights, qubit connectivity, and logical-gate implementations, allowing us to construct codes tailored to a particular hardware platform or fault-tolerant protocol. In three or more dimensions, our HCT-code family includes codes with fault-tolerant non-Clifford gates. In particular, our family subsumes previous examples of toric codes with transversal non-Clifford gates [21–23].

\*mvasmer@perimeterinstitute.ca

Published by the American Physical Society under the terms of the [Creative Commons Attribution 4.0 International](https://creativecommons.org/licenses/by/4.0/) license. Further distribution of this work must maintain attribution to the author(s) and the published article’s title, journal citation, and DOI.

Lastly, we study the problem of efficient decoding for the family of the HCT codes. We propose a decoding algorithm that connects two distinct decoders: the minimum-weight perfect-matching (MWPM) toric-code decoder [24,25] and the color-code-restriction decoder [26]. We benchmark our algorithm for two-dimensional (2D) HCT codes subject to phase-flip noise. Our decoder achieves good performance across the entire family and recovers previous results in the toric-code and color-code limits.

The remainder of this paper is structured as follows. We begin by introducing morphing and discussing a simple example in Sec. II. Then, in Sec. III, we present our first application: morphing the 15-qubit Reed-Muller code. Next, we apply morphing to color codes in Sec. IV to produce a family of HCT codes. We examine the decoding problem for HCT codes in Sec. V, where we propose and benchmark a decoder for 2D HCT codes. Finally, in Sec. VI, we summarize our results and suggest future applications of morphing.

## II. MORPHING QUANTUM CODES

Our key observation is that for a subset of the physical qubits of a stabilizer code [27], the stabilizer group induces a (smaller) stabilizer code on the qubits in the subset. Consider some stabilizer code  $\mathcal{C}$  with the stabilizer group  $\mathcal{S}$ . Let  $\mathcal{Q}$  denote the set of physical qubits of  $\mathcal{C}$  and let  $R \subseteq \mathcal{Q}$ . We define  $\mathcal{S}(R)$  to be the group generated by all the stabilizer generators of  $\mathcal{S}$  that are fully supported within  $R$ , i.e.,

$$\mathcal{S}(R) = \{P \in \mathcal{S} : \text{supp}(P) \subseteq R\}. \quad (1)$$

Since  $\mathcal{S}(R)$  is a subgroup of  $\mathcal{S}$ , it is itself an Abelian subgroup of the Pauli group not containing  $-I$  and therefore defines a stabilizer code,  $\mathcal{C}(R)$ , with physical qubits  $R$ . We refer to  $\mathcal{C}$  as the parent code and  $\mathcal{C}(R)$  as the child code.

As a stabilizer code,  $\mathcal{C}(R)$  has a Clifford encoding circuit that can be implemented with depth  $O(|R|)$  using a simple gate set of  $\{H, S, \text{cnot}\}$  (in which “CNOT” refers to “controlled-NOT.”) [27], where  $|R|$  is the size of  $R$ . Suppose that we implement the inverse of this encoding circuit. Then, the logical qubits of  $\mathcal{C}(R)$  will still be entangled with the rest of the parent code but the remaining qubits of  $\mathcal{C}(R)$  will be in a fixed (product) state and are free to be discarded [28] (assuming that we were originally in the code space of  $\mathcal{C}$ ). In effect, we have produced a new code  $\mathcal{C}_{\setminus R}$ , the physical qubits of which are the union of  $\mathcal{Q} \setminus R$  and the logical qubits of  $\mathcal{C}(R)$ . We call this procedure morphing, we call the inverse of the encoding circuit a morphing circuit, and we call  $\mathcal{C}_{\setminus R}$  the morphed code. Note that we do not necessarily anticipate implementing morphing circuits in a real device; rather, we use morphing as a systematic procedure to generate new quantum codes.

The morphed code  $\mathcal{C}_{\setminus R}$  clearly has fewer physical qubits than  $\mathcal{C}$ . But, crucially, the number of logical qubits in both codes is the same, as morphing decreases the number of physical qubits by the same amount as the number of independent stabilizer generators. However, the implementation of a subset of the logical operators of  $\mathcal{C}_{\setminus R}$  may be different to the implementation of the corresponding operators in  $\mathcal{C}$ . As  $\mathcal{S}(R) \subseteq \mathcal{S}$ , the logical operators of the parent code act as logical operators in the child code (when restricted to  $R$ ). Therefore, given the logical Pauli operators of  $\mathcal{C}(R)$ , we can compute the transformation of the logical operators of  $\mathcal{C}$  under morphing. This highlights an important degree of freedom inherent in morphing: the choice of the logical Pauli operators of the child code. All choices are equally valid but different choices can lead to different implementations of the logical operators of  $\mathcal{C}_{\setminus R}$  (see Appendix B).

We note that the code distance of  $\mathcal{C}_{\setminus R}$  may be smaller than that of  $\mathcal{C}$  and, by the same reasoning, the weight of some stabilizers of  $\mathcal{C}_{\setminus R}$  may be smaller than the corresponding stabilizers in  $\mathcal{C}$ . Less obviously, morphing can simplify the decoding problem of the parent code (see Sec. V).

In general, morphing gives us the ability to modify quantum codes, trading off various code properties against each other in order to construct a code that is suited to the constraints of a particular quantum computing platform. We now make the above discussion concrete by considering a simple example that nevertheless demonstrates many of the changes induced by morphing.

**Example 1.** Consider the Steane code [29], which has parameters  $[[7,1,3]]$  and a transversal implementation of the Clifford group. We can pick a particular subset,  $R$ , of the physical qubits of the Steane code such that  $\mathcal{C}(R)$  is the well-known  $[[4,2,2]]$  code [30] [see Fig. 1(a)]. Morphing the Steane code produces a  $[[5,1,2]]$  code with a fault-tolerant implementation of the Clifford group [see Fig. 1(b)].

## III. MAGIC STATE DISTILLATION WITH THE MORPHED REED-MULLER CODE

In an MSD protocol [16,31], one starts with some number of noisy magic states and distills these states into fewer magic states of higher quality. Magic states are used to implement challenging non-Clifford gates in fault-tolerant quantum computing architectures and hence the finding of efficient MSD protocols is an ongoing area of research [32–36]. In this section, we use our morphing procedure to construct a family of codes with applications to MSD.

### A. Morphing quantum Reed-Muller codes

Quantum Reed-Muller (QRM) codes [37,38] are a generalization of classical Reed-Muller codes [39]. We

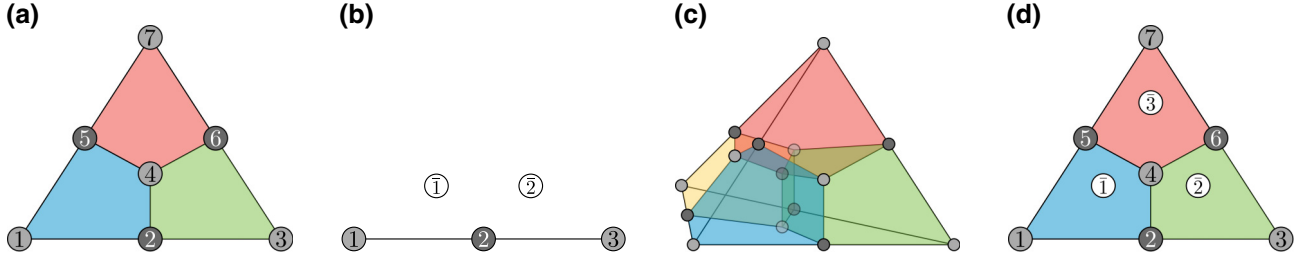


FIG. 1. (a) Steane's code. Qubits are on vertices;  $X$ - and  $Z$ -type stabilizers are on faces. (b) A  $[[5,1,2]]$  code obtained by morphing (a) with  $R$  comprising the qubits in the red face, where the corresponding child code is a  $[[4,2,2]]$  code with logical qubits  $\bar{1}$  and  $\bar{2}$ . The stabilizer group of the  $[[5,1,2]]$  code is  $\langle X_1X_2X_3, X_2X_3X_4, Z_1Z_2Z_3, Z_2Z_3Z_4 \rangle$ . To implement  $\bar{S}$ , we apply  $S^{\pm 1}$  to the light and dark gray qubits and  $CZ$  to the white qubits;  $\bar{H} = H^{\otimes 5} \text{SWAP}_{1\bar{2}}$ . (c) The  $[[15,1,3]]$  Reed-Muller code. Qubits are on vertices;  $X$ - and  $Z$ -type stabilizers are on cells and faces, respectively. (d) A  $[[10,1,2]]$  code obtained by morphing (c) with  $R$  comprising the qubits in the yellow cell, where the corresponding child code is an  $[[8,3,2]]$  code with logical qubits  $1, \bar{2}$  and  $3$ . The stabilizer group of the  $[[10,1,2]]$  code is generated by  $X_1X_2X_4X_5X_6, Z_1Z_2Z_4Z_5, Z_4Z_5Z_6$  and the analogous operators for the red and green faces. To implement  $\bar{T}$ , we apply  $T^{\pm 1}$  to the light and dark gray qubits and  $CCZ$  to the white qubits.

apply our morphing procedure to QRM codes of distance 3, where the codes in this subfamily have parameters  $[[2^{d+1} - 1, 1, 3]]$  for  $d \geq 2$ . The  $d = 2$  code is actually the Steane code discussed in Example 1. In this section, we concentrate on the  $d = 3$  code, often called the 15-qubit Reed-Muller code, which has a transversal logical  $T$  gate. We defer the discussion for general  $d$  until Appendix C.

Figures 1(c) and 1(d) illustrate the  $[[15,1,3]]$  Reed-Muller code and its morphed counterpart, a  $[[10,1,2]]$  code. One can select a subset,  $R$ , of the physical qubits of the  $[[15,1,3]]$  code such that  $\mathcal{S}(R)$  defines an  $[[8,3,2]]$  code (the so-called “smallest interesting color code” [21,40]). Morphing the  $[[15,1,3]]$  code with this subset of qubits gives a  $[[10,1,2]]$  code that inherits the logical gates of the  $[[15,1,3]]$  code and therefore has a logical  $T$  gate. This gate is not transversal (with respect to a single-qubit partition) but it is fault tolerant, as any single fault during the implementation of the gate can only lead to a detectable error.

### B. $[[10,1,2]]$ MSD protocol

Here, we compare the MSD performance of the  $[[15,1,3]]$  code with its morphed counterpart, the  $[[10,1,2]]$  code. We denote the relevant magic states by

$$\begin{aligned} |T\rangle &= T|+\rangle, \\ |CCZ\rangle &= CCZ|++++\rangle. \end{aligned} \quad (2)$$

In the 15-to-1 protocol [16], one distills 15  $|T\rangle$  states into one higher-quality  $|T\rangle$  state using the  $[[15,1,3]]$  code. However, in the 10-to-1 protocol, we instead distill seven  $|T\rangle$  and one  $|CCZ\rangle$  states into one higher-quality  $|T\rangle$  state using the  $[[10,1,2]]$  code (see Fig. 2). To our knowledge, our 10-to-1 protocol is the first example of an MSD protocol with more than one type of magic state as input.

We proceed with the standard analysis [8,16,32,41] of the 10-to-1 protocol. We assume that the only noise in the

protocol comes from the input magic states (see Fig. 2). This assumption is justified by the fact that the remaining parts of the protocol are Clifford circuits, the preparation of Pauli eigenstates, and single-qubit measurements. It is usually straightforward to make these operations fault tolerant using quantum error-correcting codes.

We start with seven copies of a mixed one-qubit state  $\rho$  such that  $\langle T | \rho | T \rangle = 1 - p$  and one mixed three-qubit state  $\tau$  such that  $\langle CCZ | \tau | CCZ \rangle = 1 - p$ , where we refer to  $p$  as the input error. We assume that  $\rho$  is diagonal in the  $|T\rangle$  basis, i.e.,

$$\rho = (1 - p) |T\rangle\langle T| + p Z |T\rangle\langle T| Z, \quad (3)$$

which can always be accomplished using Clifford twirling. We also assume that  $\tau$  has the following form:

$$\begin{aligned} \tau &= (1 - p) |CCZ\rangle\langle CCZ| \\ &+ \frac{p}{7} \sum_{\substack{\mathbf{b} \in \{0,1\}^3 \\ |\mathbf{b}| \neq 0}} Z^{\mathbf{b}} |CCZ\rangle\langle CCZ| Z^{\mathbf{b}}, \end{aligned} \quad (4)$$

where  $|\mathbf{b}|$  denotes the Hamming weight of  $\mathbf{b} = (b_1, b_2, b_3)$  and  $Z^{\mathbf{b}} = Z_1^{b_1} Z_2^{b_2} Z_3^{b_3}$ . We use this noise model because in many methods of preparing noisy  $|CCZ\rangle$  states, errors such as  $ZII$  have a comparable probability to higher-weight errors such as  $ZZZ$  [8]. In addition, as  $\{Z^{\mathbf{b}} |CCZ\rangle : \mathbf{b} \in \{0,1\}^3\}$  is an orthonormal basis, we can express a  $|CCZ\rangle$  state subject to  $X$  and  $Z$  noise as a  $|CCZ\rangle$  subject to  $Z$  noise only. Furthermore, we can eliminate the off-diagonal terms in the density matrix via Clifford twirling to bring the noisy  $|CCZ\rangle$  state into the form shown in Eq. (4) (though the coefficients may be different).

The probability that the protocol succeeds (the syndrome is trivial) is

$$p_s = 1 - 8p + 29p^2 + O(p^3). \quad (5)$$

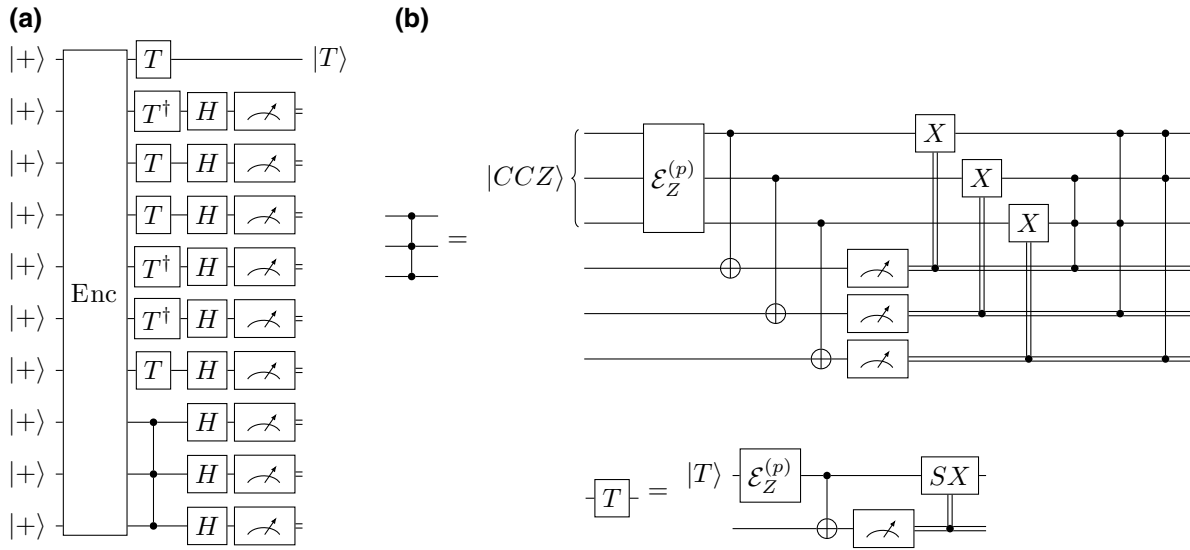


FIG. 2. (a) The  $[[10,1,2]]$  MSD protocol, consisting of the encoding circuit, noisy application of the logical  $T$  gate, and measurement. The protocol is successful if the measurements give a trivial error syndrome. The labeling of the qubits is the same as in Fig. 1(d). (b) The state injection circuits for implementing  $T$  and  $CCZ$  gates using input magic states. We assume that all components of the circuit are ideal except for the preparation of the magic states, which we model as ideal preparation followed by the noise channels implicit in Eqs. (3) and (4).

When the protocol is successful, we obtain the output state  $\rho_{\text{out}} = (1 - p_{\text{out}}) |T\rangle\langle T| + p_{\text{out}} Z |T\rangle\langle T| Z$ , where

$$p_{\text{out}} = p^2 + 9p^3 + O(p^4). \quad (6)$$

We refer to  $p_{\text{out}}$  as the output error. The leading-order prefactor in Eq. (6) is exceptionally small; in the 15-to-1 protocol, the output error is  $35p^3 + O(p^4)$  [16]. This is due

to an unusual property of the  $[[10,1,2]]$  code. Namely, for each of the seven possible  $Z^b$  errors on the input  $|CCZ\rangle$  state, there is only one logical  $Z$  operator that can be constructed by applying  $Z$  to one of the  $|T\rangle$  states.

In Fig. 3(a), we compare the performance of the 10-to-1 protocol with the 15-to-1 protocol. The success probability of the 10-to-1 protocol is always greater than or equal to the success probability of the 15-to-1 protocol and for

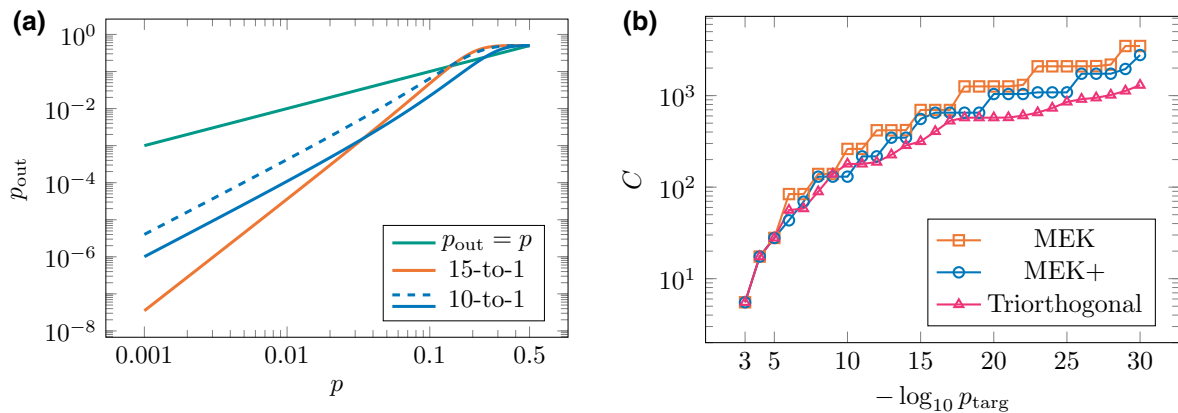


FIG. 3. (a) A plot showing the output error  $p_{\text{out}}$  as a function of the input error  $p$  for the 15-to-1 and 10-to-1 MSD protocols. The solid and dashed blue lines correspond to optimistic [Eq. (4)] and pessimistic [42] noise models for the  $|CCZ\rangle$  state, respectively. (b) A plot showing the distillation cost  $C$  for different target error rates  $p_{\text{targ}}$ , assuming an input error rate of  $p = 0.01$  and the optimistic noise model for  $|CCZ\rangle$  states. The cost for our MEK+ protocol (blue) is always smaller than the MEK protocol cost (orange) and even beats the triorthogonal protocol cost (magenta) for some values of  $p_{\text{targ}}$ .



$p \geq 0.034$ , the 10-to-1 protocol has a smaller output error. The high success probability of the 10-to-1 protocol suggests that it may be useful in early rounds of distillation, as part of a multiround protocol. To test this hypothesis, we compute the distillation cost [32]  $C$  (the expected number of magic states required) to achieve a given target error rate  $p_{\text{targ}}$ , assuming an input error rate of  $p = 0.01$ , for a number of multiround MSD protocols. Following Ref. [17], we define the Meier, Eastin, and Knill (MEK) protocol to consist of up to five rounds of distillation, where in each round either 15-to-1 [16] or 10-to-2 [17] distillation can be used. Furthermore, we define the MEK+ protocol in the same way as the MEK protocol, except that at each round we can choose between 15-to-1, 10-to-2, or 10-to-1 distillation. In Fig. 3(b), we compare the distillation costs of the MEK and MEK+ protocols with the cost of a protocol where at each round we can choose between distillation protocols based on triorthogonal codes [32]. We find that the MEK+ protocol distillation cost is always less than or equal to the MEK protocol cost and even better the triorthogonal protocol cost for  $p_{\text{targ}} \in \{10^{-6}, 10^{-9}, 10^{-10}\}$  (for the full data, including the optimal distillation sequences, see Table II in Appendix H).

One may question the reasonableness of the noise model assumed in Eq. (4), as it seems plausible that  $|CCZ\rangle$  states could be more difficult to prepare than  $|T\rangle$  states. One option for preparing  $|CCZ\rangle$  states is to use the circuit of Jones [42], which requires four  $|T\rangle$  states to produce a  $|CCZ\rangle$  state. Assuming that the  $|T\rangle$  states are as in Eq. (3), the output error of the  $[[10,1,2]]$  protocol will be  $p_{\text{out}} = 4p^2 + 21p^3 + O(p^4)$ . In this case, the distillation cost of the MEK+ protocol does not improve on the cost of the MEK protocol.

The definitive answer to the question of which MSD protocol is preferable depends on the error model of quantum computing architecture under consideration (see, e.g., Refs. [8,43]). However, simpler MSD protocols using fewer qubits are often preferable [6,43,44], which suggests that our  $[[10,1,2]]$  protocol may transpire to be useful in practice. Furthermore, we present a single example of using morphing to modify an existing MSD protocol but we conjecture that morphing could be fruitfully applied to other MSD protocols, e.g., those based on triorthogonal codes [32,36,45].

#### IV. MORPHING THE COLOR CODE

In this section, we apply our morphing procedure to the color code [18–20], a family of topological codes. We first consider 2D color codes, before discussing the generalization to three and higher dimensions. Then, we explain how morphing naturally leads to a family of HCT codes. Next, we comment on the relation of our results to previous work relating the color code and the toric code. Lastly, we

detail the fault-tolerant logical gates of HCT codes, which in three or more dimensions include non-Clifford gates.

##### A. Morphing color codes in two or more dimensions

We use the dual-lattice picture of color codes. In this picture, a 2D color-code lattice  $\mathcal{L}$  is a triangulation of a 2D manifold (possibly with boundary) the vertices of which are three colorable. That is, each vertex of the lattice can be assigned one of three colors ( $r$ ,  $g$ , or  $b$ ), such that any two vertices sharing an edge have different colors. Let  $\mathcal{L}$  denote such a lattice and let  $\mathcal{L}_0$ ,  $\mathcal{L}_1$ , and  $\mathcal{L}_2$  denote its vertices, edges, and faces, respectively. The edges and faces of the lattice inherit the colors of their vertices, e.g., an edge linking an  $r$  vertex and a  $g$  vertex is an  $rg$  edge. The qubits of the code are on the faces of  $\mathcal{L}$  and stabilizer generators are associated with interior vertices. That is, for each vertex  $v$  not on the boundary of  $\mathcal{L}$ , we have the stabilizers  $X(v) = \prod_{f \ni v} X_f$  and  $Z(v) = \prod_{f \ni v} Z_f$ , where  $X_f$  and  $Z_f$  denote Pauli  $X$  and  $Z$  operators acting on the qubit on face  $f$ , respectively, and we are implicitly interpreting faces as subsets of vertices.

To apply our morphing procedure, we need to select subsets of the color-code qubits. The subsets we choose are disklike regions of  $\mathcal{L}$  but we refer to them as ball-like in anticipation of generalization to three (and higher) dimensions. Namely, for each vertex  $v$  in  $\mathcal{L}$ , we define the ball-like region

$$\mathcal{B}^v = \bigcup_{k=0}^d \{\kappa \in \mathcal{L}_k \mid \kappa \supseteq v\}, \quad (7)$$

where  $d = 2$ . We define the color of a ball-like region  $\mathcal{B}^v$  to be the color of its central vertex  $v$ . We again use the notation  $\mathcal{B}_0^v$  to refer to the vertices of  $\mathcal{B}^v$ , etc. Restricting the stabilizer group to a ball-like region  $\mathcal{B}^v$  gives us a child code with parameters  $[[|\mathcal{B}_2^v|, |\mathcal{B}_2^v| - 2, 2]]$ , as the code has two stabilizer generators that act on all the qubits. We call such codes ball codes. In the interests of brevity, we use the phrase “morphing a ball-like region of a color code” as a shorthand for morphing a color code with the subset  $R$  of the physical qubits given by the qubits contained in a ball-like region of the code. Figure 4 shows an example of morphing a ball-like region of a 2D color code.

We now introduce a canonical geometric picture of morphing, which proves especially useful when we consider decoding HCT codes in Sec. V. The following corresponds to a particular choice of logical Pauli basis for ball codes, which we call the canonical basis (see Appendix A). We emphasize that other basis choices are equally valid and could be preferable in different contexts. Consider some ball-like region  $\mathcal{B}^v$  of a 2D color-code lattice  $\mathcal{L}$ . We note that the vertices on the boundary of  $\mathcal{B}^v$  always have two colors. When we morph  $\mathcal{B}^v$ , we remove the faces of  $\mathcal{B}^v$  from  $\mathcal{L}$  and add new edges as follows.

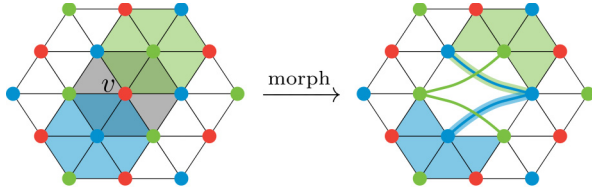


FIG. 4. Morphing a ball-like region of a 2D color code. Qubits are on triangles and stabilizers are associated with vertices. On the left, we shade the ball-like region  $\mathcal{B}^v$ , which has an associated  $[[6,4,2]]$  ball code. We also shade the support of an  $X$ -type and  $Z$ -type stabilizer in blue and green, respectively. On the right, we show the new lattice formed by morphing  $\mathcal{B}^v$ , replacing the original qubits with the four logical qubits of the ball code (blue and green edges). This changes the support of the highlighted stabilizers, as shown.

For each boundary vertex color  $c$ , we choose one of the  $c$  vertices on the boundary of  $\mathcal{B}^v$  and connect it via an edge to every other  $c$  vertex on the boundary of  $\mathcal{B}^v$ , where we refer to the new edges as  $cc$  edges. We place a qubit on each new  $cc$  edge; these qubits are the logical qubits of the ball code. In this picture, morphing takes  $X$ -type stabilizers of the parent color code to operators consisting partly of color-code  $X$ -type stabilizers and partly of toric-code  $X$ -type stabilizers—and similarly for  $Z$ -type stabilizers (for an example, see Fig. 4). We defer a detailed discussion of the canonical geometric picture (including its generalization to higher dimensions) until Appendix A.

The morphing of higher-dimensional color codes works in much the same way as the 2D case. We now briefly review the definition of the  $d$ -dimensional color code. Let  $\mathcal{L}$  be a  $d$ -dimensional lattice formed by attaching  $d$ -simplices along their  $(d-1)$ -dimensional faces. We require that the vertices of  $\mathcal{L}$  are  $(d+1)$  colorable. We place a qubit on each  $d$ -simplex of  $\mathcal{L}$  and we associate  $X$ - and  $Z$ -type stabilizer generators, respectively, with vertices and  $(d-2)$ -simplices not on the boundary of  $\mathcal{L}$ . In three dimensions (3D), qubits are on tetrahedra,  $X$ -type stabilizer generators are associated with vertices, and  $Z$ -type stabilizers are associated with edges.

In much the same way as in 2D, in higher dimensions we again morph ball-like regions of the color code. For a given vertex  $v \in \mathcal{L}_0$ , the  $d$ -dimensional ball-like region  $\mathcal{B}^v$  consists of all simplices that contain  $v$ , alongside  $v$  itself [see Eq. (7)]. Figure 5 shows an example of such a ball-like region in a 3D color code. Restricting the stabilizer group of the color code to a ball-like region  $\mathcal{B}^v$  gives us a  $d$ -dimensional ball code, which we characterize in the following lemma (the proof of which we defer until Appendix A).

**Lemma 2.** *The ball code defined on the  $d$ -dimensional ball-like region  $\mathcal{B}^v$  has parameters*

$$N = |\mathcal{B}_d^v|, \quad K = |\mathcal{B}_1^v| - d, \quad D = 2. \quad (8)$$

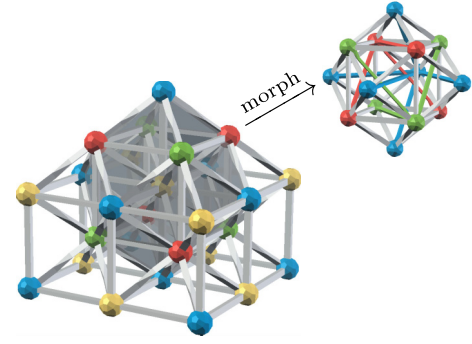


FIG. 5. Morphing a ball-like region of a 3D color code. Qubits are on tetrahedra;  $X$  and  $Z$  stabilizers are associated with vertices and edges, respectively. We shade a ball-like region (with an associated  $[[24,11,2]]$  ball code) and show its transformation under morphing.

We note that the canonical geometric picture can be generalized to higher dimensions (see Fig. 5 and Appendix A).

## B. Hybrid color-toric codes

We use morphing to construct a family of HCT codes in  $d$  dimensions, for  $d \geq 2$ . Given an initial color code defined on a lattice  $\mathcal{L}$ , we obtain different HCT codes by morphing subsets of the ball-like regions of  $\mathcal{L}$ . Concretely, suppose that  $\mathcal{L}$  is a closed manifold and consider the case where we morph a fraction  $q \in [0, 1]$  of  $r$  ball-like regions (the choice of color is arbitrary). For  $q = 0$ , we of course have the original color code and for  $q = 1$ , we obtain  $d$  copies of the toric code (up to adding or removing ancilla qubits). Let  $\tilde{\mathcal{L}}$  denote the HCT-code lattice produced from  $\mathcal{L}$  via morphing. For  $q = 1$ , qubits will be exclusively associated with edges, as all the original color-code qubits were contained in some  $r$  ball-like region of  $\mathcal{L}$ . As we show in Appendix A, the  $X$ - and  $Z$ -type stabilizers of  $\tilde{\mathcal{L}}$  can be partitioned into  $d$  subgroups such that each subgroup only contains operators acting on  $cc$  edges, where  $c$  is any of the  $d+1$  colors except for  $r$ . In 2D, each of these subgroups defines a toric code but in higher dimensions to obtain toric codes we need to introduce ancillas, unless we consider lattices with special structure (see Appendix D). We can also consider the case where we morph a fraction  $q$  of all the ball-like regions in  $\mathcal{L}$  but then we need to be careful because ball-like regions of different colors can overlap (see Sec. V).

In  $d \geq 3$  dimensions, color codes have transversal non-Clifford gates [19,21,46–49], which our HCT codes inherit. As we show in Appendix B, if a  $d$ -dimensional color code has a transversal non-Clifford logical operator  $L$  implemented by  $R_d^{\pm 1}$  gates, then HCT codes obtained from this code will have a fault-tolerant logical operator  $L$  implemented by  $R_d^{\pm 1}$  and multicontrol- $Z$  gates. We recall that  $R_d = \exp(i\pi/2^d Z)$  and that the  $d$ -qubit multicontrol- $Z$  gate is specified by its action on the states in the computational

basis, namely

$$MCZ |b_1, \dots, b_d\rangle = \left(1 - 2 \prod_{i=1}^d b_i\right) |b_1, \dots, b_d\rangle. \quad (9)$$

We now consider some examples of HCT codes with fault-tolerant non-Clifford gates. The  $[[10,1,2]]$  code introduced in Sec. III A is one such example, as the  $[[15,1,3]]$  code fits into the color-code family [47]. Furthermore, we can construct a HCT code with a fault-tolerant logical  $R_d$  gate from any color code defined on a cellulation of a  $d$ -simplex. Another example is given by the family of hypercubic color codes [21], which we illustrate in Fig. 6. Hypercubic color codes have transversal logical  $MCZ$  gates and therefore HCT codes obtained from these codes have fault-tolerant logical  $MCZ$  gates.

We now briefly discuss how our results relate to previous work. In Ref. [21], the authors have proved that the  $d$ -dimensional color code is local-Clifford equivalent to  $d$  copies of the  $d$ -dimensional toric code. Their argument is nonconstructive, i.e., they show that for a  $d$ -dimensional color code defined on a lattice  $\mathcal{L}$ , there exists a Clifford isometry that transforms the color code into  $d$  copies of the toric code. Furthermore, the isometry has the following form:

$$V = \bigotimes_{\substack{u \in \mathcal{L}_0 \\ \text{col}(u)=c}} V_u, \quad (10)$$

where  $V_u$  is a Clifford isometry acting on the physical qubits of the color code in the neighborhood of the vertex  $u$ . Morphing can be understood as giving an explicit implementation of the local Clifford isometry  $V$ , as each morphing circuit is a Clifford isometry applied in the neighborhood of a vertex. In Refs. [50] and [22], the

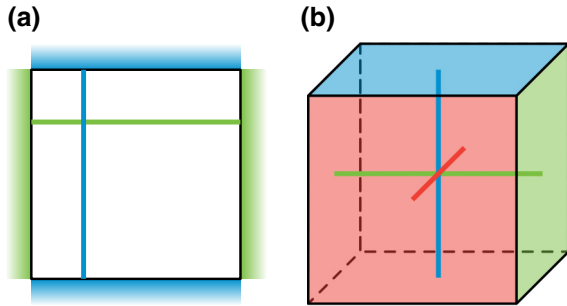


FIG. 6. Hypercubic color codes are defined on lattices that tessellate the hypercube, where opposite boundaries have the same color. (a) The  $d = 2$  case. Logical  $X_1$  and  $Z_2$  are supported on the green line (as products of  $X$  and  $Z$  operators, respectively). Similarly,  $X_2$  and  $Z_1$  are supported on the blue line. (b) The  $d = 3$  case. Logical  $X$  operators are supported on the boundaries and the corresponding logical  $Z$  operators connect boundaries of the same color.

authors show that one can obtain color codes by concatenating multiple toric codes with small error-detecting codes. This is a special case of morphing, but in reverse. In Refs. [22] and [23], the authors present constructions of 3D and four-dimensional (4D) toric codes with transversal logical  $MCZ$  gates. We can use morphing to recover these results, as we explain in Appendix D.

## V. DECODING HCT CODES

In this section, we propose an efficient decoding algorithm for 2D HCT codes and we numerically benchmark its performance. Remarkably, our decoder reduces to the MWPM decoder [24,25] in one limit and to the restriction decoder in the opposite limit. We recall that the restriction decoder is an efficient decoder of the color code in  $d \geq 2$  dimensions that builds upon the ideas in Refs. [51] and [52].

### A. Decoding algorithm

We consider phase-flip noise, as the correction of bit flips is analogous and can be done separately. Let  $\tilde{\mathcal{L}}$  denote a 2D HCT-code lattice, produced from a color-code lattice  $\mathcal{L}$  (without boundary) by morphing some subset of its ball-like regions. We label the three colors of the vertices by  $r, b$ , and  $g$ . We use the canonical geometric picture from Sec. IV A, so qubits in  $\tilde{\mathcal{L}}$  are associated with  $rgb$  faces, i.e., faces  $f \in \tilde{\mathcal{L}}_2 \cap \mathcal{L}_2$  and  $cc$  edges, i.e., edges  $e \in \tilde{\mathcal{L}}_1 \setminus \mathcal{L}_1$ . Furthermore,  $X$ -type stabilizer generators are associated with vertices  $v \in \mathcal{L}_0$ . We emphasize that  $\tilde{\mathcal{L}}$  should not be treated as a topological object but, rather, as a combinatorial object. We also make use of a well-known concept in color-code decoding: restricted lattices [18,26]. Let  $\mathcal{L}^{c_1 c_2}$  be the lattice formed from  $\tilde{\mathcal{L}}$  by deleting all vertices of color  $c \neq c_1 \neq c_2$ , along with all edges and faces that contain these vertices.

We can now state our decoding problem: given an error syndrome  $\sigma \subseteq \tilde{\mathcal{L}}_0$  caused by an unknown phase-flip error  $\epsilon \subseteq (\tilde{\mathcal{L}}_2 \cap \mathcal{L}_2) \cup (\tilde{\mathcal{L}}_1 \setminus \mathcal{L}_1)$ , output a correction operator  $\zeta \subseteq (\tilde{\mathcal{L}}_2 \cap \mathcal{L}_2) \cup (\tilde{\mathcal{L}}_1 \setminus \mathcal{L}_1)$  with the same syndrome as  $\epsilon$ . Decoding is successful if  $\zeta$  and  $\epsilon$  differ by a stabilizer. Our decoding algorithm consists of the following three steps:

- (1) *Matching.* We use MWPM to pair up the vertices of  $\sigma$  in the restricted lattices  $\tilde{\mathcal{L}}^{rg}$  and  $\tilde{\mathcal{L}}^{rb}$ . That is, we obtain a set of edges  $E^{rg} \subseteq \tilde{\mathcal{L}}_1^{rg}$  the boundary of which is exactly  $\sigma \cap \tilde{\mathcal{L}}_0^{rg}$  (and similarly for  $\tilde{\mathcal{L}}^{rb}$ ). In a slight abuse of terminology, we call such a set of edges a matching.
- (2) *Local modification.* We modify the matchings as follows, focusing on  $E^{rg}$  (for  $E^{rb}$  exchange  $g \leftrightarrow b$  below). For each  $rr$  edge  $e \in E^{rg}$ , we find the color  $c$  of its corresponding ball-like region  $\mathcal{B}^v$  in  $\mathcal{L}$ . If  $c \neq g$ , we remove  $e$  from the matching. Let  $u_1$  and  $u_2$  be the endpoints of  $e$ . We find two vertices  $w_1, w_2 \in$

$\tilde{\mathcal{L}}_0$  such that  $(u_1, w_1, v)$  and  $(u_2, w_2, v)$  are contained in  $\mathcal{L}_2$  for some  $v \in \mathcal{L}_0$ . Then, we find a path  $(e_1, \dots, e_m)$  from  $w_1$  to  $w_2$  consisting of  $gg$  edges. We add the edges  $(u_1, w_1), (u_2, w_2), e_1, \dots, e_m$  to the matching.

- (3) *Local lift.* First, we add each  $cc$  edge in the combined matching  $E^{rg} \cup E^{rb}$  to the correction  $\zeta$ . Then, for each  $r$  vertex  $v \in e$  such that  $e \in E^{rg} \cup E^{rb}$ , we apply a local lift. For regions of  $\tilde{\mathcal{L}}$  that are the same as the corresponding regions of  $\mathcal{L}$ , the local lift is the color-code lift described in Ref. [26]. In the morphed regions of  $\tilde{\mathcal{L}}$ , the local lift must be modified to account for the changes due to morphing (see Appendix G). Let  $\zeta_v \subseteq (\tilde{\mathcal{L}}_2 \cap \mathcal{L}_2) \cup (\tilde{\mathcal{L}}_1 \setminus \mathcal{L}_1)$  be the output of the local lift at  $v$ . We update the correction  $\zeta = \zeta \triangle \zeta_v$ .

Figure 7 illustrates our algorithm via an example and a C++ implementation of our algorithm (utilizing BLOSSOM V [53]) is available online [54]. We can now explain our earlier statement that morphing can simplify the decoding problem. Morphing (applied judiciously) transforms a color code into copies of the toric code, changing the decoding problem from color-code decoding to the simpler toric-code decoding problem. In particular, the local lift in the toric-code regions is trivial compared with the local lift in the color-code regions. Therefore, one can argue that the decoding problem is simplified in the regions of the lattice that have been morphed.

Our algorithm has run-time complexity  $O(N^3)$  (see Appendix G), where  $N$  is the number of physical qubits in the code, due to the MWPM subroutine. As with the restriction decoder, MWPM can be replaced with

any algorithm for 2D toric-code decoding. For example, replacing MWPM with UNION-FIND [55] would give our algorithm almost linear time complexity. We note that our decoder is an instance of the “decoding using emergent symmetries” paradigm, which underlies many topological code decoders [26,56,57]. As in the color code, the emergent symmetries in our case are the products of all stabilizers of the same color.

One example application for our decoder is color-code–toric-code lattice surgery [58]. There can be advantages to preparing magic states in a color code before transferring them to a toric code [59]. This transfer is accomplished via lattice surgery, during which the color code and toric code are temporarily merged to form a HCT code that must be decoded as part of the lattice-surgery protocol. For our decoder to be directly applicable to this situation, we would need to modify our algorithm to work for codes with boundaries, but we expect that this modification would proceed in a similar way to the restriction decoder [60].

## B. Numerics

We investigate the performance of our decoding algorithm using Monte Carlo simulations. We begin with the family of 2D color codes defined on  $L \times L$  triangular tilings, where six triangles meet at each vertex. We use periodic boundary conditions, i.e., we identify the coordinates  $(x, y) = (x + L, y) = (x, y + L) = (x + L, y + L)$ . From this starting point, we explore three ways of constructing HCT codes:

- (1) *Method A.* We choose  $q \in [0, 1]$  and construct a random HCT code by morphing each  $r$  ball-like region

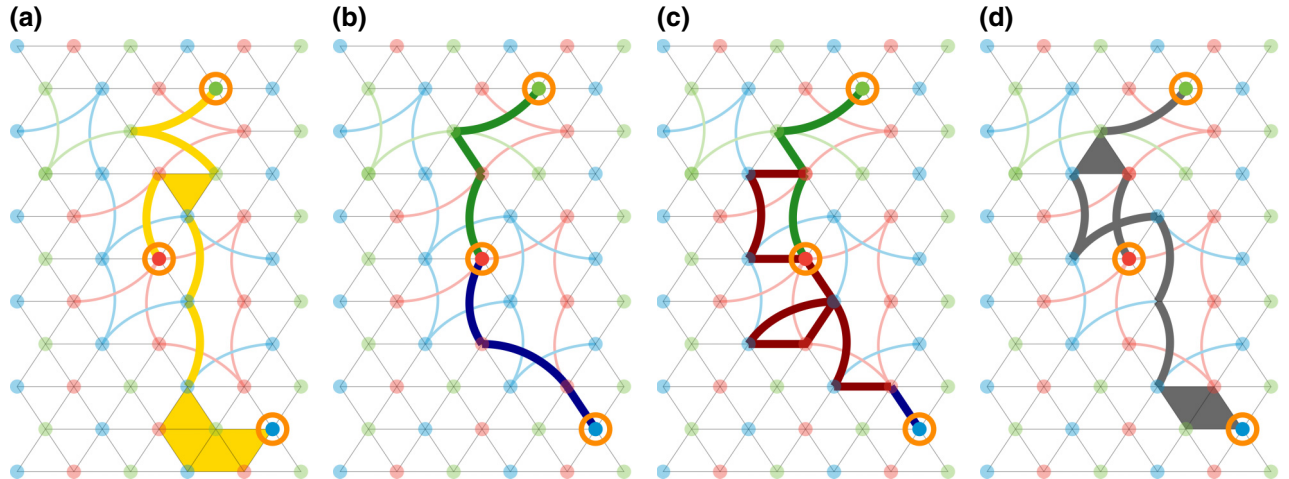


FIG. 7. An illustration of our decoding algorithm for HCT codes. (a) A phase-flip error (yellow faces and edges) and its syndrome (ringed vertices). (b)–(d) The three steps of the HCT-code decoder: (1) matching—use MWPM to compute a matching (dark green and blue edges) of the syndrome in the restricted lattices  $\tilde{\mathcal{L}}^{rg}$  and  $\tilde{\mathcal{L}}^{rb}$ ; (2) local modification—locally modify the matching (new edges included in the matching are highlighted in red); (3) local lift—use the local-lifting procedure to compute a correction (gray faces and edges) from the modified matching.



with probability  $q$ . We consider both choosing the same logical Pauli basis for each region (A1) and choosing the basis randomly (A2).

- (2) *Method B.* We choose  $q \in [0, 1]$  and iterate through the  $r$  ball-like regions, morphing with probability  $q$ . Next, we iterate through the  $g$  ball-like regions and morph with probability  $q$ , except if an overlapping region has already been morphed. Lastly, we iterate through the  $b$  ball-like regions and morph with probability  $q$  (again unless an overlapping region has already been morphed). In all cases, we choose the logical Pauli basis randomly.
- (3) *Method C.* We choose  $q \in [0, 1]$  and put the vertices of the lattice into a random order. For each vertex in the list, with probability  $q$  we morph the ball-like region centered at the vertex (choosing the logical Pauli basis randomly), except if an overlapping region has already been morphed.

By definition, the parameter  $q$  captures the proportion of morphed  $r$  ball-like regions in methods A1, A2, and B. However, in method C the parameter  $q$  does not correspond directly to the proportion of morphed ball-like regions because of the nonoverlapping condition. Furthermore, in the  $q = 1$  limit, Methods A1, A2, and B all produce toric codes with certainty, whereas method C with high probability does not produce a toric code, as this would require all the vertices of one color to occur at the start of the random ordering.

We investigate the performance of our decoder as a function of  $q$  for each of the above methods. In each case, we use an error model where independent identically distributed (IID)  $Z$  errors affect the qubits with probability  $p$  and stabilizer measurements are perfect. We use Monte Carlo simulations to estimate the logical error rate  $p_{\text{fail}}$  as a function of  $p$ ,  $L$ , and  $q$  [see Fig. 8(a)]. For each value

of  $q > 0$ , we randomly generate 100 HCT-code lattices for each  $L$ , and for each value of  $p$  we carry out 1000 Monte Carlo trials per lattice. For each value of  $q$ , we estimate the error threshold  $p_{\text{th}}(q)$  using finite-size scaling methods [61], as illustrated in Fig. 8(b).

For method A1, we reproduce the known color-code error threshold of  $p_{\text{fail}}(0) \approx 0.085$  [52] and the known toric-code threshold of  $p_{\text{fail}}(1) \approx 0.103$  [62]. The threshold monotonically increases from  $q = 0$  to  $q = 1$  [see Fig. 8(c)]. For method A2, we observe an increased threshold of  $p_{\text{fail}}(1) \approx 0.105$  [see Fig. 8(c)]. This is not surprising, as by picking the logical Pauli basis randomly, we are highly unlikely to produce the standard square-lattice toric code for  $q = 1$ .

For method B, we observe similar results to the case where we morph only  $r$  ball-like regions using random logical Pauli bases. For method C, we find that the error threshold does not vary with  $q$  and is approximately equal to the color-code error threshold of  $p_{\text{fail}}(0) \approx 0.085$ . The data for these cases are shown in Fig. 8(c).

## VI. CONCLUSIONS

In this paper, we introduce morphing as a systematic method for modifying quantum codes. By applying morphing to quantum Reed-Muller codes, we obtain a family of codes with fault-tolerant non-Clifford gates and applications in MSD. We find that in the case of the color code, morphing allows us to change the implementation of fault-tolerant logical gates, reduce the weight of stabilizers and the number of physical qubits (at the cost of also reducing the code distance), and simplify the decoding problem. One can apply morphing to tetrahedral color codes [19,46,49] to construct HCT codes with a fault-tolerant logical  $T$  gate. The  $[[10,1,2]]$  code is actually

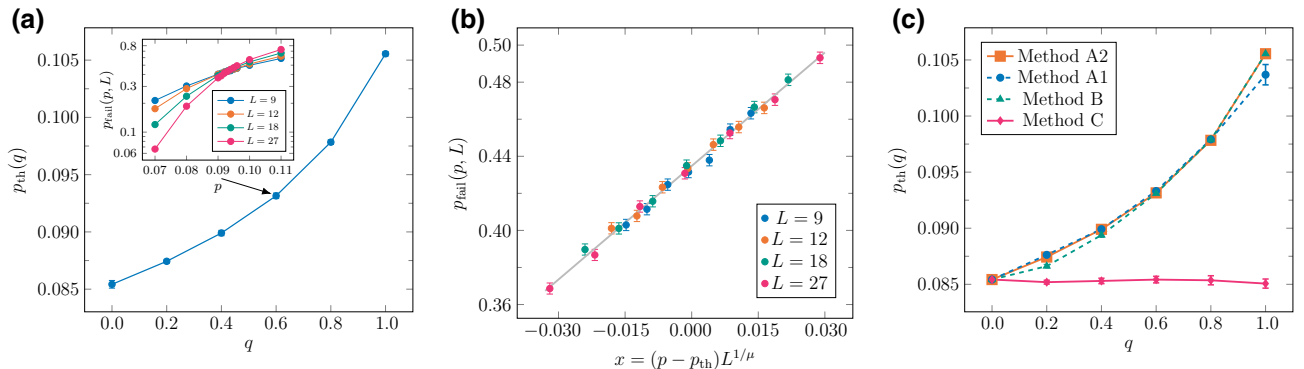


FIG. 8. (a) A plot of the error threshold  $p_{\text{th}}$  as a function of  $q$  for the ensemble of HCT codes produced using method A1. The inset shows a plot of the logical error rate  $p_{\text{fail}}$  as a function of the phase-flip error rate  $p$  for  $q = 0.6$ . (b) The rescaled data for the inset in (a), using finite-size scaling analysis to estimate the threshold. The fitting parameters for the collapse are  $p_{\text{th}} = 0.0932(1)$  and  $\mu = 1.42(8)$  and the gray line shows a quadratic fit. (c) A comparison of the behavior of the error threshold as a function of  $q$  for different methods of constructing HCT codes.



the smallest example of this family, which is thoroughly explored in Refs. [63,64].

We examine the decoding problem for 2D HCT codes and we detail an efficient decoding algorithm based on existing toric-code and color-code decoders. Our decoding algorithm achieves good performance across the whole family and we expect that our approach should generalize to higher dimensions. A natural next step would be to study more realistic noise models that include measurement errors. We expect that in this case, standard techniques such as repeating the stabilizer measurements [65,66] would work for HCT codes. In addition, it would be interesting to investigate the optimal error threshold of 2D HCT codes using tensor-network decoders [67,68]. We expect that the optimal threshold will interpolate between the optimal thresholds of the color code and the derived toric codes. This would potentially explain why the optimal threshold of the color code defined on the triangular lattice [69] matches the optimal threshold of the toric code defined on the square lattice [70–72], as the latter can be obtained from the former via morphing.

Morphing can be straightforwardly generalized to stabilizer subsystem codes [73]. We again select a subset of the physical qubits of the subsystem code and consider the code generated by all the stabilizers of the subsystem code that are fully supported within the subset. We remark that we cannot instead choose gauge operators supported within the subset, as then some of the logical operators of the subsystem codes may not act as logical operators in the child code. We expect that it may be interesting to apply morphing to, e.g., the gauge color code [46,47], in order to define a HCT-code family interpolating between the gauge color code and the recently introduced 3D subsystem toric code [74].

Lastly, we expect that morphing could be fruitfully applied to triorthogonal codes [32] and pin codes [75], two families of codes that generalize color codes in different ways. We conjecture that morphing may allow us to improve the performance of MSD protocols based on triorthogonal codes (especially when mixing different input magic states) and to modify pin codes in much the same way as we do in the case of color codes.

## ACKNOWLEDGMENTS

M.V. thanks Dan Browne, Simon Burton, and Chris Chubb for insightful discussions and Raymond Laflamme for valuable comments on an earlier draft of this paper. A.K. acknowledges funding provided by the Simons Foundation through the “It from Qubit” Collaboration. This work was completed prior to A.K. joining the AWS Center for Quantum Computing. Research at Perimeter Institute is supported in part by the Government of Canada through the Department of Innovation, Science and Economic

Development Canada and by the Province of Ontario through the Ministry of Colleges and Universities.

## APPENDIX A: MORPHING $d$ -DIMENSIONAL COLOR CODES

In this appendix, we explain how to morph  $d$ -dimensional color codes. We begin by fixing the notation and reviewing the definitions of the toric code and the color code (Appendix A 1). Then, in Appendix A 2, we examine the regions of the color code to which we apply our morphing procedure: colorable  $d$ -balls. Finally, in Appendix A 3, we introduce a family of HCT codes, which we construct by morphing the color code.

### 1. Preliminaries

A  $d$ -dimensional lattice  $\mathcal{L}$  can be constructed by attaching  $d$ -dimensional cells to one another along their  $(d - 1)$ -dimensional faces. We denote the  $k$ -cells of a lattice  $\mathcal{L}$  by  $\mathcal{L}_k$ . We say that an  $m$ -cell  $\mu \in \mathcal{L}_m$  is contained in a  $k$ -cell  $\kappa \in \mathcal{L}_k$  and we write  $\mu \subseteq \kappa$ , if the vertices of  $\mu$  are a subset of the vertices of  $\kappa$  (where  $m \leq k$ ). We define the  $n$ -star of a  $k$ -cell  $\kappa \in \mathcal{L}_k$  to be  $\text{St}_n(\kappa) = \{\nu \in \mathcal{L}_n \mid \kappa \subseteq \nu\}$ .

The lattices that we consider may have a boundary, denoted by  $\partial\mathcal{L}$ , which comprises all  $(d - 1)$ -cells of  $\mathcal{L}$  that are contained in a single  $d$ -cell, along with all  $k$ -cells contained in these  $(d - 1)$ -cells, for  $0 \leq k \leq d - 2$ . We denote the interior of a lattice by  $\mathcal{L}^\circ = \mathcal{L} \setminus \partial\mathcal{L}$  and we denote the internal  $k$ -cells by  $\mathcal{L}_k^\circ = \mathcal{L}_k \cap \mathcal{L}^\circ$ .

We often consider lattices the cells of which are simplices and the vertices of which are  $(d + 1)$  colorable, i.e., one can introduce a function

$$\text{col} : \mathcal{L}_0 \rightarrow [d + 1], \quad (\text{A1})$$

such that for any two vertices  $u$  and  $v$  sharing an edge,  $\text{col}(u) \neq \text{col}(v)$  and we use the shorthand  $[n] = \{1, 2, \dots, n\}$ . Such a lattice is called a  $d$ -colex [76]. We abuse the notation and write  $\text{col}(\kappa) = \bigcup_{v \subseteq \kappa} \text{col}(v)$  for some  $k$ -simplex  $\kappa$ , i.e., the color of  $\kappa$  is the set of the colors of its vertices. We denote the subset of  $k$ -cells in  $\mathcal{L}$  of color  $c$  by  $\mathcal{L}_k^c = \{\kappa \in \mathcal{L}_k \mid \text{col}(\kappa) = c\}$ . Given two simplices  $\mu \in \mathcal{L}_m$  and  $\nu \in \mathcal{L}_n$ , we define their join  $\mu * \nu$  to be the smallest simplex in  $\mathcal{L}$  that contains them both. If no such simplex exists, we define their join to be empty.

Anticipating the definition of the color code, we now introduce generalized boundary operators. Given a lattice  $\mathcal{L}$ , let  $C_k(\mathcal{L})$  be a vector space over  $\mathbb{F}_2$  with a basis given by the  $k$ -cells of  $\mathcal{L}$ . Subsets of  $k$ -cells are consequently isomorphic to vectors in  $C_k(\mathcal{L})$ . For all  $k \neq n$ , we define the generalized boundary operator  $\partial_{k,n}$  as a linear map specified for every basis element  $\kappa \in \mathcal{L}_k$  as

$$\partial_{k,n}\kappa = \begin{cases} \sum_{v \subseteq \kappa} v, & \text{for } k > n, \\ \sum_{v \supseteq \kappa} v, & \text{for } k < n. \end{cases} \quad (\text{A2})$$

We note that the “standard” boundary operator  $\partial_k = \partial_{k,k-1}$  is a special case of the generalized boundary operator.

### a. Toric codes and color codes

We now review the definition of the toric code [24, 77, 78] in  $d$  dimensions, where  $d \geq 2$ . Let  $\mathcal{L}$  be a  $d$ -dimensional lattice with boundary  $\partial\mathcal{L}$ . We divide  $\partial\mathcal{L}$  into two subsets, the “rough” boundaries  $\partial\mathcal{L}^{(R)}$  and the “smooth” boundaries  $\partial\mathcal{L}^{(S)}$ . We place a qubit on each edge in  $\mathcal{L}_1 \setminus \partial\mathcal{L}_1^{(R)}$ . The stabilizer of the code is

$$\mathcal{S} = \langle X(v), Z(f) \mid v \in \mathcal{L}_0 \setminus \partial\mathcal{L}_0^{(R)}, f \in \mathcal{L}_2 \setminus \partial\mathcal{L}_2^{(R)} \rangle, \quad (\text{A3})$$

where  $X(v) = \prod_{e \ni v} X_e$ ,  $Z(f) = \prod_{e \subseteq f} Z_e$ ,  $Z_e$  denotes a Pauli  $Z$  operator acting on the qubit on edge  $e$  and  $X_e$  denotes a Pauli  $X$  operator acting on the qubit on edge  $e$ . For a face  $f$  adjacent to a rough boundary, the set of edges contained in  $f$  may include edges with no associated qubits. In this case, we define  $Z_e$  to be the identity.

The other important family of codes for us is the family of color codes [18, 21, 76]. Let  $\mathcal{L}$  be a  $(d \geq 2)$ -colex, with boundary  $\partial\mathcal{L}$ . The color code defined on  $\mathcal{L}$  has qubits on  $d$ -cells,  $X$ -type stabilizer generators associated with internal vertices, and  $Z$ -type stabilizer generators associated with internal  $(d-2)$ -simplices. That is, the stabilizer group of the code is

$$\mathcal{S} = \langle X(v), Z(\mu) \mid v \in \mathcal{L}_0^\circ, \mu \in \mathcal{L}_{d-2}^\circ \rangle, \quad (\text{A4})$$

where  $U(\kappa) = \prod_{\delta \in \text{St}_d(\kappa)} U_\delta$  and  $U_\delta$  means  $U$  applied to the qubit on the  $d$ -simplex  $\delta \in \mathcal{L}_d$ . This notation clashes with the notation used for toric codes above, but it should always be clear from context what kind of code we are referring to.

### 2. Ball codes

Let  $\mathcal{L}$  be a  $d$ -colex and pick a vertex  $v \in \mathcal{L}_1$ . We define the colorable  $d$ -ball  $\mathcal{B}^v$  centered at  $v$  to be

$$\mathcal{B}^v = \bigcup_{k=0}^d \{\kappa \in \mathcal{L}_k \mid \kappa \supseteq v\}, \quad (\text{A5})$$

i.e.,  $\mathcal{B}^v$  is the union of all  $k$ -simplices in  $\mathcal{L}$  that contain  $v$ . We define the boundary of  $\mathcal{B}^v$  as follows:

$$\partial\mathcal{B}^v = \bigcup_{k=0}^d \{\kappa \in \mathcal{L}_k \setminus \mathcal{B}_k^v \mid \exists \delta \in \mathcal{B}_d^v : \delta \supseteq \kappa\}. \quad (\text{A6})$$

Namely,  $\partial\mathcal{B}^v$  consists of all the  $k$ -simplices of  $\mathcal{L}$  that are contained in a  $d$ -simplex of  $\mathcal{B}^v$  but are not themselves contained in  $\mathcal{B}^v$ . We use  $\mathcal{B}_k^v$  to denote the set of  $k$ -simplices contained in  $\mathcal{B}^v$ , with the obvious extension to  $\partial\mathcal{B}^v$ . We

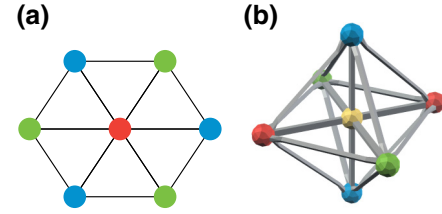


FIG. 9. (a) A colorable 2-ball and its boundary. The colorable 2-ball consists of the central  $r$  vertex and all simplices containing it. The boundary consists of the  $b$  and  $g$  vertices, alongside the edges connecting them. (b) A 3D colorable 3-ball and its boundary. The colorable 3-ball consists of the central yellow vertex and all simplices containing it. The boundary consists of the  $r$ ,  $g$ , and  $b$  vertices, alongside the triangles and edges the vertices of which are subsets of these vertices.

define the color of a colorable  $d$ -ball  $\mathcal{B}^v$  to be  $\text{col}(v)$ . Figure 9 shows some example colorable  $d$ -balls in 2D and 3D.

When we morph a color code, we pick the subset of qubits  $R$  (see Sec. II) to be the qubits contained in a colorable  $d$ -ball  $\mathcal{B}^v$ . The corresponding code has the stabilizer

$$\mathcal{S}_{\mathcal{B}^v} = \langle X(v), Z(\mu) \mid \mu \in \mathcal{B}_{d-2}^v \rangle. \quad (\text{A7})$$

This is exactly the stabilizer group of a color code defined on a  $d$ -colex  $\mathcal{B}^v \cup \partial\mathcal{B}^v$  with boundary  $\partial\mathcal{B}^v$  [recall Eq. (A4)]. We call such a code a “ball code.” We now come to our first lemma about ball codes.

**Lemma 2.** *The ball code defined on the  $d$ -dimensional ball-like region  $\mathcal{B}^v$  has parameters*

$$N = |\mathcal{B}_d^v|, \quad K = |\mathcal{B}_1^v| - d, \quad D = 2. \quad (8)$$

*Proof.* As the ball code defined on  $\mathcal{B}_v$  is a color code, we immediately have  $N = |\mathcal{B}_d^v|$ .

To find  $K$ , we first observe that one can define a  $(d-1)$ -dimensional color code on  $\partial\mathcal{B}^v$ , which we call the boundary code. In the boundary code, qubits are on  $(d-1)$ -simplices,  $X$ -type stabilizers are associated with vertices, and  $Z$ -type stabilizers are associated with  $(d-3)$ -simplices. There is an isomorphism between the  $k$ -simplices of  $\mathcal{B}^v$  and the  $(k-1)$ -simplices of  $\partial\mathcal{B}^v$ , for  $1 \leq k \leq d$ . We have  $\kappa \cong \tau$  for  $\kappa \in \mathcal{B}_k^v$  and  $\tau \in \partial\mathcal{B}_{k-1}^v$ , if  $\kappa = \tau * v$ . Furthermore, the  $Z$ -type stabilizers of the ball code and the boundary code have the same support, because  $\text{St}_d(\kappa) = \text{St}_d(\tau)$  for  $\kappa = \tau * v$ . In particular, independent  $Z$ -type stabilizer generators of the ball code correspond to independent  $Z$ -type stabilizer generators of the boundary code.

As the boundary code is a color code defined on a  $(d-1)$ -colex that is homeomorphic to a  $(d-1)$ -sphere,

it encodes no logical qubits. Let  $\mathcal{S}_{\mathcal{B}^v}^Z$  and  $\mathcal{S}_{\partial\mathcal{B}^v}^Z$  denote the  $Z$ -type stabilizer groups of the ball and boundary codes, respectively (and analogously for the  $X$ -type stabilizer groups). We have

$$N = \text{rank } \mathcal{S}_{\mathcal{B}^v}^Z + \text{rank } \mathcal{S}_{\partial\mathcal{B}^v}^X = \text{rank } \mathcal{S}_{\mathcal{B}^v}^Z + \text{rank } \mathcal{S}_{\mathcal{B}^v}^X + K. \quad (\text{A8})$$

Solving for  $k$ , we obtain

$$K = \text{rank } \mathcal{S}_{\partial\mathcal{B}^v}^X - 1, \quad (\text{A9})$$

as  $\text{rank } \mathcal{S}_{\mathcal{B}^v}^Z = \text{rank } \mathcal{S}_{\partial\mathcal{B}^v}^Z$  and  $\text{rank } \mathcal{S}_{\mathcal{B}^v}^X = 1$ .

The  $X$ -type stabilizer generators of the boundary code are associated with the vertices of  $\partial\mathcal{B}^v$  and every  $(d-1)$ -simplex of  $\partial\mathcal{B}^v$  contains exactly  $d$  vertices, each with a different color. Consequently, we have  $(d-1)$  independent relations between subsets of  $X$ -type stabilizer generators, namely

$$\prod_{\substack{u \in \mathcal{B}_0^v \\ \text{col}(u)=2}} X(u) = \prod_{\substack{u \in \mathcal{B}_0^v \\ \text{col}(u)=3}} X(u) = \dots = \prod_{\substack{u \in \mathcal{B}_0^v \\ \text{col}(u)=d+1}} X(u), \quad (\text{A10})$$

where we assume, without loss of generality, that  $\text{col}(v) = 1$ . This gives  $\text{rank } \mathcal{S}_{\partial\mathcal{B}^v}^X = |\partial\mathcal{B}_0^v| - (d-1)$  and substituting into Eq. (A9) gives the desired result.

Finally, we come to the code distance  $D$ . As ball codes are Calderbank-Steane-Shor (CSS) codes [29,79], we need only consider logical operators that are tensor products of  $X$  and  $I$  or tensor products of  $Z$  and  $I$ . We note that  $X(e)$  is a logical  $X$  operator of the ball code, where  $e \in \mathcal{B}_1^v$ . This operator is clearly not a stabilizer but it commutes with the stabilizers of the ball code. To see this, consider a  $Z$ -type stabilizer generator  $Z(\mu)$ , where  $\mu \in \mathcal{B}_{d-2}^v$ . The overlap of  $X(e)$  and  $Z(\mu)$  (the qubits on which they both act nontrivially) is given by  $\text{St}_d(\mu * e)$ . The join of  $\mu$  and  $e$  is empty, equal to  $\mu$  (if  $e \subseteq \mu$ ), or equal to a  $(d-1)$ -simplex of  $\mathcal{B}^v$ . In each case,  $|\text{St}_d(\mu * e)| = 0 \pmod 2$  [see the (Even Support) Lemma 4 in Ref. [47]].

The ball code has a single  $X$ -type stabilizer acting on all its physical qubits, so any weight-2  $Z$  operator commutes with the stabilizers of the ball code. Consider the operator  $Z(\lambda)$ , where  $\lambda \in \mathcal{B}_{d-1}^v$ .  $Z(\lambda)$  has weight 2, as each  $(d-1)$ -simplex of  $\mathcal{B}^v$  is contained in exactly two  $d$ -simplices. For any such operator, we can always find a logical  $X$  operator  $X(e)$  such that  $e * \lambda = \delta \in \mathcal{B}_D^v$ , i.e.,  $Z(\lambda)$  and  $X(e)$  anticommute. Therefore,  $Z(\lambda)$  is a logical  $Z$  operator and consequently the ball code has a  $Z$ -distance of 2. The  $X$ -distance is also at least 2, as each qubit is in the support of two or more  $Z$ -type stabilizers. ■

We now specify a canonical generating set for the logical Pauli operators of a ball code defined on  $\mathcal{B}^v$ . Following

on from the proof of Lemma 2, we choose the following generating set for the logical  $X$  operators:

$$\mathcal{X} = \bigcup_{c \in [d+1] \setminus \text{col}(v)} \{X(e) \mid e \in \mathcal{B}_1^v \setminus e_c^* : \text{col}(e) = c\}, \quad (\text{A11})$$

where  $e_c^*$  is some edge of color  $c$  that we are free to choose. Namely, our generating set consists of operators  $X(e)$  for each edge  $e$  in  $\mathcal{B}^v$ , except for one edge,  $e_c^*$ , of each color  $c \neq \text{col}(v)$ . We choose each operator  $X(e)$  in our generating set to act on a single logical qubit and we define the color of a logical qubit to be the color of its associated edge. This implies that the operator  $X(e_c^*)$  implements a logical  $X$  on all logical qubits of color  $c$ . The set  $\mathcal{Z} = \{Z(\lambda) \mid \lambda \in \mathcal{B}_{d-1}^v\}$  generates the logical  $Z$  operators of the ball code (see Lemma 2). The action of these operators is fixed via commutation. Concretely, the logical operator  $Z(\lambda)$  acts nontrivially on the logical qubits with associated logical operators  $X(e)$  such that  $|\text{St}_d(\lambda) \cap \text{St}_d(e)| = 1$  (or, equivalently,  $\lambda * e = \delta \in \mathcal{B}_d^v$ ).

We now examine some examples of ball codes. The ball code defined on the colorable 2-ball shown in Fig. 9(a) is a  $[[6,4,2]]$  code and the ball code defined on the colorable 3-ball shown in Fig. 9(b) is an  $[[8,3,2]]$  code. This code is exactly the so-called “smallest interesting color code” [40,47] and it is part of a family of color codes, which we call hyperoctahedron codes.

**Example 3 (Hyperoctahedron codes).** A hyperoctahedron (also called a cross polytope) is the  $d$ -dimensional generalization of the octahedron and can be constructed as follows. In  $d$ -dimensional Euclidean space, place vertices at all the permutations of  $(\pm 1, 0, 0, \dots, 0)$ . The  $d$ -hyperoctahedron is the convex hull of these vertices. We remark that the  $k$ -cells of the  $d$ -hyperoctahedron are  $k$ -simplices, for  $0 \leq k < d$ . Let  $\mathcal{O}$  denote the  $d$ -hyperoctahedron, which we transform into a colorable  $d$ -ball as follows. First, we create a vertex  $v$  in the center of  $\mathcal{O}$ . Next, for each  $k$ -simplex  $\kappa$  of  $\mathcal{O}$ , we add the  $k$ -simplex  $\kappa * v$ , for  $1 \leq k \leq d$ . The result is a colorable  $d$ -ball, with  $\mathcal{B}^v$  comprising the simplices that contain  $v$  and  $\partial\mathcal{B}^v$  consisting of the original simplices of  $\mathcal{O}$ . The hyperoctahedron code is then simply the ball code defined on  $\mathcal{B}_v$ . Hyperoctahedron codes generalize the  $[[4,2,2]]$  code [30] and the aforementioned  $[[8,3,2]]$  code (the dual of a  $d$ -hyperoctahedron is a  $d$ -hypercube). The parameters of the  $d$ -hyperoctahedron code are  $[[2^d, d, 2]]$ , as can be derived from Eq. (8) and the fact that a  $d$ -hyperoctahedron has  $2d$  vertices and  $2^d (d-1)$ -cells. We note that for  $d$ -hyperoctahedron codes, there is no freedom in the choice of canonical logical Pauli basis, as there is only one logical qubit of each color.

**Example 4** (3D ball codes). One can construct colorable 3-balls by taking the dual of Archimedean solids the faces of which all have an even number of sides. The polyhedra satisfying these restrictions are the truncated octahedron, the truncated cuboctahedron, and the truncated icosidodecahedron. The corresponding ball codes have parameters  $[[24,11,2]]$  (this is the code shown in Fig. 5),  $[[48,23,2]]$  and  $[[120,59,2]]$ , respectively. Each of these codes will have logical  $CCZ$ -type gates (see Theorem 5) implemented by physical  $T^{\pm 1}$  gates and could therefore be used to distill magic states. The associated MSD protocol has asymptotic average overhead  $O(\log^\gamma(1/\epsilon))$  as the output error  $\epsilon \rightarrow 0$ , where  $\gamma = \log(n/k)/\log(d)$ . The ball codes described above have  $\gamma$  values close to 1, especially the  $[[120,59,2]]$  code, where  $\gamma = 1.02$ . This is significant as it has previously been conjectured that  $\gamma \geq 1$  for all MSD protocols [32] and the only known protocols with  $\gamma < 1$  require either many (approximately  $2^{58}$ ) qubits [34] or large (41) local qudit dimension [80].

### 3. Hybrid color-toric codes

Using our morphing procedure, we construct a family of HCT codes. Namely, we start with a color code and morph a subset of its colorable  $d$ -balls to obtain a HCT code. We note that we use the phrase “morphing a colorable  $d$ -ball” as a shorthand for morphing a color code with the subset  $R$  of the physical qubits given by the qubits contained in a colorable  $d$ -ball. The HCT-code family contains the color code and copies of the toric code but also contains codes with regions of toric code and regions of color code. We now explain how the parameters of a HCT code change when we morph a colorable  $d$ -ball  $\mathcal{B}_v$ , which allows us to derive the parameters of any HCT code (by starting from the parent color code). Suppose that the initial HCT code has parameters  $[[N,K,D]]$ . Then, after morphing the colorable  $d$ -ball  $\mathcal{B}_v$ , the resultant code has parameters

$$\begin{aligned} N' &= N - |\mathcal{B}_d^v| + |\mathcal{B}_1^v| - d, \\ K' &= K, \\ D' &\geq D - \max_{e \in \mathcal{B}_1^v} |\text{St}_d(e)| + 1. \end{aligned} \quad (\text{A12})$$

We now briefly justify Eq. (A12). The value for  $N'$  follows directly from Lemma 2. As we discuss in Sec. II, the number of encoded qubits remains the same, as we lose the same number of physical qubits and independent stabilizer generators. Finally, the code distance decreases because some logical operators (acting on two or more physical qubits) of the ball code will be mapped to single-qubit operators by morphing. The highest-weight generator of the logical Pauli group of the ball code defined on  $\mathcal{B}^v$  is the logical  $X$  operator of highest weight (the  $Z$  operators are weight 2), i.e.,  $X(e^*)$ , where  $e^* = \arg \max_{e \in \mathcal{B}_1^v} |\text{St}_d(e)|$ . Importantly, for color codes,  $\max_{e \in \mathcal{B}_1^v} |\text{St}_d(e)|$  is a constant

that does not scale with the size of the code, so the code distance remains macroscopic.

In the remainder of this appendix, we introduce a geometric picture of morphing and we show that the HCT-code family contains toric codes.

#### a. Geometric picture of morphing

We begin by introducing a canonical geometric picture of morphing, which enables us to see the connection to toric codes more clearly. Let  $\mathcal{B}^v$  be a colorable  $d$ -ball of a  $d$ -colex  $\mathcal{L}$  and assume that  $\text{col}(v) = d + 1$ . When morphing  $\mathcal{B}^v$ , we represent our choice of logical Pauli basis pictorially by removing  $\mathcal{B}_v$  from  $\mathcal{L}$  and creating new edges linking vertices of the same color in  $\partial \mathcal{B}^v$ . Let  $u \in \partial \mathcal{B}_0^v$  be the endpoint of the edge  $e_c^*$  [recall Eq. (A11)] on the boundary of  $\mathcal{B}^v$ . We add edges connecting  $u$  to all the other vertices of color  $c$  on the boundary of  $\mathcal{B}^v$  and we place physical qubits on these new edges. We refer to these new qubits as edge qubits and we refer to the original color-code qubits as simplex qubits. We use  $\tilde{\mathcal{L}}$  to denote the HCT-code lattice produced from  $\mathcal{L}$  according to the above procedure. Also, we note that we must modify the generalized boundary operators to reflect the changes to the lattice structure; for a concrete example of this, see Appendix G.

This geometric picture enables us to continue to associate the  $X$ -type stabilizer generators of a HCT code with vertices. Concretely, the  $X$ -type stabilizer associated with a vertex  $u \in \tilde{\mathcal{L}}_0$  is

$$X(u) = \prod_{\delta \supseteq u} X_\delta \prod_{\substack{e \supseteq u \\ \text{col}(e) = \{c,c\}}} X_e, \quad (\text{A13})$$

where  $c = \text{col}(u)$ ,  $\delta \in \tilde{\mathcal{L}}_d$ , and  $e \in \tilde{\mathcal{L}}_1$  has an associated edge qubit. This last point is guaranteed by the condition that  $\text{col}(e) = \{c, c\}$  as, unlike the edges of  $\mathcal{L}$ , the edges created during morphing connect vertices of the same color. Figure 10 shows the intersection of a color-code  $X$ -type stabilizer with a colorable 3-ball.

The  $Z$ -type stabilizers of a HCT code can also be understood using our geometric picture, though the definition is more obscure. We continue to associate HCT-code  $Z$ -type stabilizer generators with  $(d - 2)$ -cells, as follows:

$$Z(\mu) = \prod_{\delta \supseteq \mu} Z_\delta \prod_{\substack{e = (u,v) \\ u \in \partial_{d-1,0} \partial_{d-2,d-1} \mu \\ \text{col}(e) = \{c,c\}}} Z_e, \quad (\text{A14})$$

where  $\delta \in \tilde{\mathcal{L}}_D$ , and  $c = \text{col}(u)$ . To unpack Eq. (A14), we note that  $\partial_{d-2,d-1} \mu$  comprises the  $(d - 1)$ -simplices of  $\tilde{\mathcal{L}}$  that contain  $\mu$  and that  $\partial_{d-1,0} \partial_{d-2,d-1} \mu$  consists of the vertices contained in an odd number of these  $(d - 1)$ -simplices.



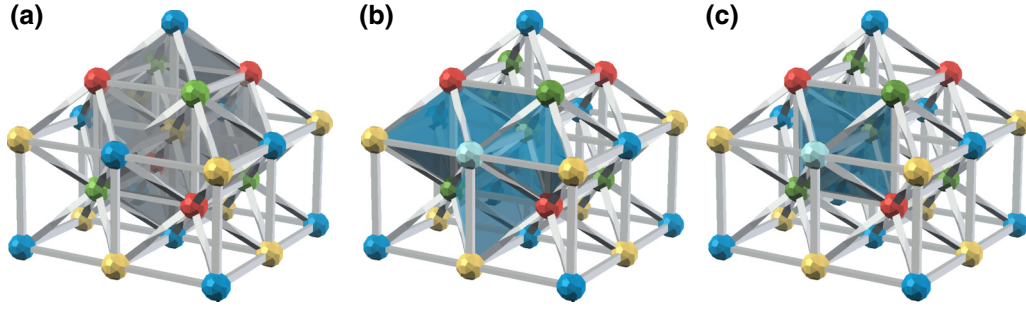


FIG. 10. (a) We show part of a 3-colex with a colorable 3-ball highlighted in gray. (b) We highlight (shaded blue tetrahedra) the support of the  $X$ -type stabilizer associated with the light blue vertex. (c) We show the intersection of the support of the stabilizer (b) with the colorable 3-ball (a). These qubits comprise the support of the ball-code logical  $X$  operator that is associated with the edge linking the light blue vertex and the central yellow vertex.

### b. Toric codes as HCT codes

In this appendix, we sketch an argument that the HCT-code family contains copies of the toric code. Let  $\mathcal{L}$  be a  $d$ -colex defined on a closed manifold. Suppose that we morph every colorable  $d$ -ball of color  $r = d + 1$  in  $\mathcal{L}$ . In the resultant HCT code, no stabilizer generators will be associated with  $r$  vertices and the only physical qubits will be edge qubits, as all simplex qubits will have been removed during morphing. The  $X$ -type stabilizers of the HCT code can be partitioned into disjoint subgroups,  $\langle X(v) \mid v \in \tilde{\mathcal{L}}_0 : \text{col}(v) = c \rangle$ , for  $c \in [d]$ . This is because each generator  $X(v)$  now acts exclusively on edge qubits of color  $\{c, c\}$ .

As there are no remaining  $r$  vertices, given a  $(d - 2)$ -cell  $\mu \in \tilde{\mathcal{L}}_{d-2}$ , the color of any  $(d - 1)$ -cell  $\lambda \in \tilde{\mathcal{L}}_{d-1}$  such that  $\lambda \supseteq \mu$  is fixed. Therefore, the  $Z$ -type stabilizers of the HCT code can also be partitioned into disjoint subgroups indexed by  $c \in [d]$ , where the operators in each subgroup only act on qubits of color  $\{c, c\}$ . To summarize, for  $c \in [d]$ , the stabilizer group of the HCT code can be partitioned into  $d$  disjoint subgroups of the form

$$\langle X(v), Z(\mu) \mid v \in \tilde{\mathcal{L}}_0, \mu \in \tilde{\mathcal{L}}_{d-2} : \text{col}(v) = c, \text{col}(\mu) = [d] \setminus \{c\} \rangle. \quad (\text{A15})$$

When restricted to the  $cc$  edges of  $\tilde{\mathcal{L}}$ , the  $X$ -type stabilizer generators of the  $c$ -subgroup have the form  $X(v) = \prod_{e \supseteq v} X_e$ , i.e., they are toric-code  $X$ -type stabilizers [recall Eq. (A3)]. Now consider some  $Z$ -type stabilizer  $Z(\mu)$  in the  $c$ -subgroup. Recalling Eq. (A14), we first write  $\partial_{d-2, d-1} \mu = \{\lambda_1, \lambda_2, \dots, \lambda_m\}$ . In  $\mathcal{L}$ , each  $\lambda_i$  must have been contained in the boundary of two colorable  $d$ -balls of color  $d + 1$ ; otherwise, the  $\lambda_i$  would have been removed during morphing. Therefore,  $\lambda_i = \mu * u_i$ , where  $\text{col}(u_i) = c$ . Suppose that we permute our labeling of the  $\lambda_i$  such that, in  $\mathcal{L}$ ,  $\lambda_i$  and  $\lambda_{i+1}$  (evaluated modulo  $m + 1$ ) are on the boundary of the same colorable  $d$ -ball  $\mathcal{B}^v$ , where  $\text{col}(v) = r$ . Then, either  $(u_i, u_{i+1})$  is in the support of  $Z(\mu)$  or  $(u_i, w)$  and  $(w, u_{i+1})$  are in the support of  $Z(\mu)$  for some  $w$  that was

also contained in  $\partial \mathcal{B}^v$ . Consequently, the support of  $Z(\mu)$  is a cycle of  $cc$  edges, i.e., it has the form of a toric-code  $Z$ -type stabilizer [recall Eq. (A3)].

In 2D, we can see that the HCT-code family contains toric codes by inspection, e.g., by applying the transformation shown in Fig. 4 to all  $r$  colorable 2-balls. In higher dimensions, generic examples become more complex, with the exception of a family of HCT codes derived from color codes with special structure, which we examine in Appendix D.

## APPENDIX B: NON-CLIFFORD GATES IN $d$ -DIMENSIONAL HCT CODES

Color codes have a multitude of transversal logical gates implemented  $R_d$  gates, including non-Clifford gates in  $d \geq 3$  dimensions [18, 19, 21, 46–49]. To describe the implementation of these gates, we note that the qubits of a color code are bipartite in the following sense. We can divide the  $d$ -simplices of a  $d$ -colex into two disjoint sets, such that any two  $d$ -simplices that share a  $(d - 1)$ -simplex are in different sets. We denote these sets by  $T$  and  $T^c$  and for a single-qubit unitary  $U$ , we write  $U(T)$  to denote the application of  $U$  to all of the qubits in  $T$ . Every  $d$ -dimensional color code has a transversal logical gate implemented by  $\tilde{R}_d = R_d(T)R_d^\dagger(T^c)$ . The logical action of this gate depends on the topology of the colex. For example, in tetrahedral color codes  $\tilde{R}_3$  implements a logical  $R_3$  gate [19, 46, 49]. Also, in the family of hypercubic color codes (see Fig. 6),  $\tilde{R}_d$  implements the logical  $d$ -qubit MCZ gate [47], which we denote by  $C_d$ .

HCT codes inherit the logical gates of their parent color codes. To find the implementation of a non-Clifford gate in a HCT code, we investigate how morphing changes the implementation of the corresponding color-code logical gate. This entails understanding the transversal logical gates of ball codes, which is the topic of the next subsection.



### 1. MCZ gates in ball codes

As ball codes are color codes, they have transversal logical gates that are implemented by  $R_d$  gates. Any unitary can be expanded in the Pauli basis, so in principle we can compute the logical action of any transversal gate in a ball code by expanding the transversal gate in the Pauli basis and then grouping terms by logical Pauli. However, this is cumbersome to do in practice, so instead we characterize the transversal logical gates of the ball-code family.

First, we introduce some notation. Let  $\kappa \in \mathcal{B}_k^v$  be a  $k$ -simplex of a colorable  $d$ -ball  $\mathcal{B}_v$ , where  $0 \leq k \leq D$ . We write

$$\tilde{U}(\kappa) = \prod_{\delta \in \text{St}_d(\kappa) \cap T} U(\delta) \prod_{\delta \in \text{St}_d(\kappa) \cap T^c} U^\dagger(\delta). \quad (\text{B1})$$

The group commutator of two unitary operators  $A$  and  $B$  is defined to be  $K[A, B] = ABA^\dagger B^\dagger$ . We note the identities  $K[R_k, X] = R_{k-1}$  and  $K[C_k, X] = C_{k-1}$ .

**Theorem 5.** *Let  $\mathcal{B}^v$  be a colorable  $d$ -ball with an associated ball code, where  $d \geq 2$ , and let  $\kappa \in \mathcal{B}_{d-k}^v$  be a  $(d-k)$ -simplex of  $\mathcal{B}_v$ , where  $k \in [d]$ . The operator  $\tilde{R}_k(\kappa)$  implements a logical  $C_k$  gate on all  $k$ -tuples of logical qubits the corresponding edges  $e_j \in \mathcal{B}_1^v$  of which have the following property:*

$$e_1 * \dots * e_k * \kappa = \delta \in \mathcal{B}_d^v, \quad (\text{B2})$$

i.e., the join of the edges and  $\kappa$  is a  $d$ -simplex of  $\mathcal{B}^v$ .

*Proof.* We prove the theorem by induction on  $k$ .

*Base case ( $k=1$ ).* Suppose that we apply the operator  $\tilde{R}_1(\lambda)$  for some  $\lambda \in \mathcal{B}_{d-1}^v$ . Up to an unimportant global phase,  $\tilde{R}_1(\lambda)$  is a logical  $Z$  operator of the ball code. Consider a single-qubit logical  $X$  operator  $X(e)$ , where  $e \in \mathcal{B}_1^v$ .  $\tilde{R}_1(\lambda)$  and  $X(e)$  commute if  $\text{St}_d(\lambda) \cap \text{St}_d(e) = \emptyset$  or if  $e \subseteq \lambda$ . In the second case, we have that  $\text{St}_d(\lambda) \subseteq \text{St}_d(e)$  and as  $|\text{St}_d(\lambda)| = 2$ , the operators commute. Crucially, in both cases  $(e * \lambda)$  is not a  $d$ -simplex of  $\mathcal{B}^v$ . If  $e \not\subseteq \lambda$  and their intersection is nonempty, we must have  $|\text{St}_d(\lambda) \cap \text{St}_d(e)| = 1$ , i.e., both  $\lambda$  and  $e$  are contained in the same  $d$ -simplex or, equivalently,  $(e * \lambda) = \delta \in \mathcal{B}_d^v$ .

*Inductive step.* Suppose that we apply the operator  $\tilde{R}_{k+1}(\mu)$ , where  $\mu \in \mathcal{B}_{d-k-1}^v$ . We first show that  $\tilde{R}_{k+1}(\mu)$  preserves the stabilizer. We only need to check the single  $X$ -type stabilizer  $X(v)$ , as  $\tilde{R}_{k+1}(\mu)$  trivially commutes with the  $Z$ -type stabilizers. Consider the group commutator

$$K[\tilde{R}_{k+1}(\mu), X(v)] = \tilde{R}_{k+1}(\mu) X(v) \tilde{R}_{k+1}^\dagger(\mu) X(v) = \tilde{R}_k(\mu). \quad (\text{B3})$$

We can partition the support of  $\tilde{R}_k$  as follows:

$$\text{St}_d(\mu) = \bigsqcup_{\kappa \in \text{St}_{d-k}^c(\mu)} \text{St}_d(\kappa), \quad (\text{B4})$$

where  $\text{St}_{d-k}^c(\mu) = \{\kappa \in \mathcal{B}_{d-k}^v \mid \mu \subseteq \kappa, \text{col}(\kappa) = c\}$ , and  $c$  is a any subset of  $[d+1]$  of cardinality  $d-k+1$  with  $\text{col}(\mu) \subseteq c$ . Consequently, we can rewrite Eq. (B6) as follows:

$$K[\tilde{R}_{k+1}(\mu), X(e)] = \prod_{\kappa \in \text{St}_{d-k}^c(\mu)} R_k(\kappa). \quad (\text{B5})$$

By the inductive assumption,  $R_k(\kappa)$  implements a logical  $C_k$  gate on all  $k$ -tuples of logical qubits the corresponding edges  $e_j \in \mathcal{B}_1^v$  of which are such that  $(e_1 * \dots * e_k * \kappa) = \delta \in \mathcal{B}_d^v$ . Crucially,  $\text{col}(e_j) \not\subseteq c$  for all  $j \in [k]$ . Without loss of generality, suppose that  $\text{col}(\mu) = [d-k]$  and  $\text{col}(v) = 1$ . Then, one possible choice for  $c$  is  $[d-k+1]$ . In this case,  $\prod_{\kappa \in \text{St}_{d-k}^c(\mu)} R_k(\kappa)$  acts on logical qubits with colors in the set  $\{(1, d-k+2), \dots, (1, d+1)\}$ . If we instead choose  $c$  to be a different subset of  $[d+1]$ , then  $\prod_{\kappa \in \text{St}_{d-k}^c(\mu)} R_k(\kappa)$  will act on logical qubits with a different set of colors. There are  $k+1$  possible choices for  $c$  and there is no common color of logical qubit in the  $k+1$  corresponding sets of logical qubits. Therefore, the only way in which Eq. (B5) can hold for all choices of  $c$  is if  $\prod_{\kappa \in \text{St}_{d-k}^c(\mu)} R_k(\kappa) = 1$ .

Now, we consider the group commutator of  $\tilde{R}_{k+1}(\mu)$  with  $X(e)$ , where  $e \in \mathcal{B}_1^v$ . If  $\text{St}_d(\mu) \cap \text{St}_d(e) = \emptyset$ , then  $K[\tilde{R}_{k+1}(\mu), X(e)] = 1$ , as the operators have disjoint support. Now suppose that  $\text{St}_d(\mu) \cap \text{St}_d(e) \neq \emptyset$ . If  $\text{St}_d(\mu) \subseteq \text{St}_d(e)$ , then  $e \subseteq \mu$  and

$$K[\tilde{R}_{k+1}(\mu), X(e)] = \tilde{R}_k(\mu) = 1, \quad (\text{B6})$$

by the same argument as in the previous paragraph. The final case to consider is when  $\text{St}_d(\mu) \cap \text{St}_d(e) \neq \emptyset$  and  $\text{St}_d(\mu) \not\subseteq \text{St}_d(e)$ . Observe that  $\text{St}_d(\mu) \cap \text{St}_d(e) = \text{St}_d(e * \mu)$ , as every  $d$ -simplex that contains  $\mu$  and  $e$  must also contain their join. Therefore,

$$K[\tilde{R}_{k+1}(\mu), X(e)] = \tilde{R}_k(e * \mu), \quad (\text{B7})$$

where  $(e * \mu) = \kappa \in \mathcal{B}_{d-k}^v$ . By the inductive assumption,  $\tilde{R}_k(\kappa)$  implements a logical  $C_k$  gate on all  $k$ -tuples of logical qubits the corresponding edges  $e_j \in \mathcal{B}_1^v$  of which are such that  $(e_1 * \dots * e_k * \kappa) = \delta \in \mathcal{B}_d^v$ . This completes the proof, as the group commutator of  $C_{k+1}$  and a single-qubit  $X$  is  $C_k$ . ■

We remark that if we choose  $k = d$  in Theorem 5, we obtain a logical circuit consisting of  $d$ -qubit MCZ gates, implemented by  $\tilde{R}_d(v)$ , i.e., the gate acts on all the physical

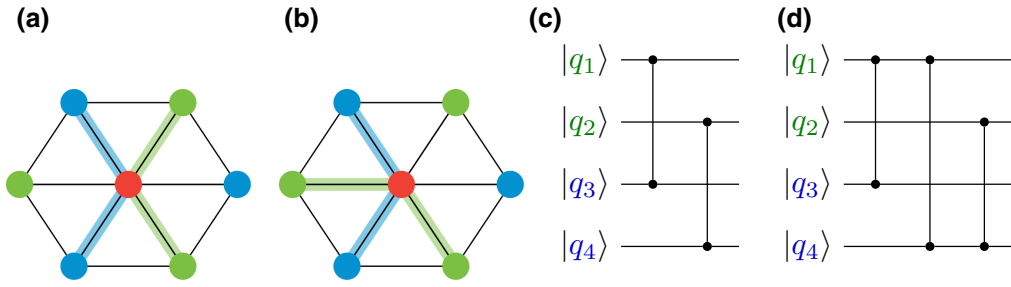


FIG. 11. Logical gates implemented by  $\tilde{R}_2(v)$  in a  $[[6,4,2]]$  code. (a) One choice of logical Pauli basis, where for each highlighted edge  $e$  we have a logical operator  $X(e)$  with the labeling (clockwise from the top left)  $\bar{X}_3, \bar{X}_1, \bar{X}_2$ , and  $\bar{X}_4$ . Here, two subsets of logical operators have corresponding edges the join of which is a triangle. (b) A different choice of logical Pauli basis, where clockwise from the top left we have  $\bar{X}_3, \bar{X}_2, \bar{X}_4$ , and  $\bar{X}_1$ . Here, three subsets of logical operators have corresponding edges the join of which is a triangle. (c), (d) The logical operator implemented by  $\tilde{R}_2(v)$  for (a) and (b), respectively.

qubits of the code. Figure 11 shows some example logical circuits implemented by  $\tilde{R}_2$  for the  $[[6,4,2]]$  code. A particularly simple application of Theorem 5 is to hyperoctahedron codes. For the  $d$ -dimensional hyperoctahedron code, it can be easily verified that  $\tilde{R}_d(v)$  implements a  $C_d$  gate on the  $d$  logical qubits of the code. Moreover, for  $k \in [d]$  and  $\kappa \in \mathcal{B}_{d-k}^v$ ,  $\tilde{R}_k(\kappa)$  implements a  $C_k$  gate on the  $k$  logical qubits of color  $c \notin \text{col}(\kappa)$ .

Theorem 5 allows us to characterize the implementation of the logical HCT-code gates that are inherited from the parent color code. If the parent color code has a logical gate implemented by  $\tilde{R}_d$ , then HCT codes derived from this code will have the same logical gate implemented by  $R_d, R_d^\dagger$ , and  $C_d$  gates. For each morphed colorable  $d$ -ball, Theorem 5 tells us the specific  $C_d$  circuit to apply. More concretely, for a ball code with parameters  $[[N, K, D]]$ , the  $C_d$  circuit will have depth at most  $\binom{N}{d}$ . As the size of any ball-like region is bounded, the implementation of the logical HCT-code gate will be of constant depth and hence fault tolerant. In Appendices C–F, we consider families of HCT codes where the  $C_d$  circuits for each ball-like region have simple structure.

### APPENDIX C: FURTHER DETAILS ON MORPHED QRM CODES

We begin this appendix by briefly reviewing the color-code construction of distance-3 QRM codes [47]. We start with a  $d$ -simplex and place another  $d$ -simplex inside of it. We color the vertices of each simplex with colors  $c \in [d+1]$  such that each vertex of the same simplex has a different color. For each vertex  $v$  of the internal simplex, we connect  $v$  to all vertices of the external simplex the color of which is different from  $\text{col}(v)$ . The  $d$ -dimensional color code defined on this lattice is the  $d$ -dimensional QRM code of distance 3. Figure 12 shows the lattices for the 2D and 3D codes.

Now, suppose that we morph a colorable  $d$ -ball of QRM( $d$ ). We observe that all ball codes in QRM( $d$ ) are  $d$ -hyperoctahedron codes. This is because a given internal vertex  $v$  has  $d$  neighbors in the internal simplex and  $d$  neighbors in the external simplex, where there are exactly two neighbors of each color, and all neighbors are connected to each other except for those of the same color. Therefore, the  $(d-1)$ -dimensional surface

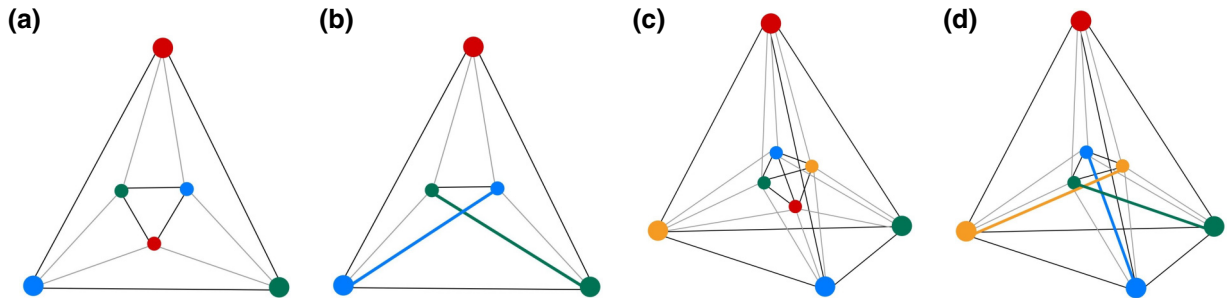


FIG. 12. QRM codes and their morphed counterparts. (a) QRM(2), more commonly known as the Steane code. Qubits are on triangles and stabilizer generators are associated with internal vertices. (b) The  $[[5,1,2]]$  code produced by morphing the colorable 2-ball centered at the internal  $r$  vertex. Four qubits are replaced by two (the blue and green edges). (c) QRM(3), more commonly known as 15-qubit Reed-Muller code. Qubits are on tetrahedra and  $X$ -type ( $Z$ -type) stabilizer generators are associated with internal vertices (edges). (d) The  $[[10,1,2]]$  code produced by morphing the colorable 3-ball at the internal  $r$  vertex. Eight qubits are replaced by three (the blue, green, and yellow edges).

of any internal colorable  $d$ -ball in  $\text{QRM}(d)$  is exactly a  $d$ -hyperoctahedron. The parameters of the morphed  $\text{QRM}(d)$  code are  $\llbracket 2^d + d - 1, 1, 2 \rrbracket$  and it has a fault-tolerant logical  $R_d$  gate. The logical  $R_d$  gate of the morphed code has the same implementation as in  $\text{QRM}(d)$  for the remaining simplex qubits, along with a  $C_d$  gate on the edge qubits.

For MSD protocols of the type discussed in Sec. III B, the leading-order term in the output error is  $ap^D$ , where  $D$  is the distance of the code and  $a$  is the number of logical  $Z$  operators of weight  $D$ . For  $\text{QRM}(d)$ ,  $a = (1 - 2^{d+1})(1 - 2^d)/3$ , whereas in the corresponding morphed  $\text{QRM}$  code  $a = d$  (as we prove shortly), so there is an exponential separation between the leading-order prefactors as the spatial dimension increases.

**Lemma 6.** *The morphed  $\text{QRM}(d)$  code has  $d$  logical  $Z$  operators of weight 2.*

*Proof.* Any weight-2 logical  $Z$  operator of the morphed  $\text{QRM}(d)$  code must act on one or more edge qubits as the distance of  $\text{QRM}(d)$  is 3. Consider an edge of color  $c$  and suppose that we apply a  $Z$  operator to the qubit on this edge. To form a weight-2 logical  $Z$  operator, the only possible choice for the second qubit is the  $d$ -simplex spanned by the internal vertex of color  $c$  and the vertices on the boundary the colors of which are not equal to  $c$ . To see this, observe that the Pauli  $Z$  acting on the edge qubit anticommutes with the  $X$ -type stabilizer generator associated with the internal endpoint of the edge. The only other qubit that is contained in the support of this  $X$ -type stabilizer generator and no other  $X$ -type stabilizer generators is the one described above, as all other  $d$ -simplices contain internal vertices of color not equal to  $c$ . Therefore, any other choice will lead to more unsatisfied stabilizers. Also, any weight-2  $Z$  operator acting exclusively on edge qubits will not satisfy two stabilizers (associated with the internal endpoints of the edges). In the morphed  $\text{QRM}(d)$  code there are  $d$  edges with associated qubits, so there are  $d$  corresponding logical  $Z$  operators of weight 2. ■

#### APPENDIX D: CONSTRUCTING COLOR CODES AND TORIC CODES FROM COXETER DIAGRAMS

In this appendix, we describe a construction of color codes and toric codes from Coxeter diagrams [81]. Such an approach has been employed before in Refs. [75,82] and is a generalization of the Schläfli symbol construction used in Refs. [23,83–85]. Coxeter diagrams are used to represent Coxeter groups, which describe the symmetries of polytopes and tessellations in terms of reflections. A tessellation is a gapless covering of a manifold by uniform polytopes such that each adjacent pair of polytopes

share a facet [a  $(d - 1)$ -cell]. We say that a tessellation is uniform if all of its vertices are identical, i.e., there is the same combination of polytopes at each vertex. We also say that a tessellation is regular if it is uniform and all the polytopes are identical. A Coxeter group is defined by the group presentation

$$\langle r_1, r_2, \dots, r_m : (r_i r_j)^{p_{ij}} = 1 \rangle, \quad (\text{D1})$$

where  $p_{i,i} = 1$  (as the  $r_i$  are reflections),  $p_{i,j} \geq 2$  for  $i \neq j$ , and  $p_{i,j} = \infty$  implies that the relation is ignored.

Each Coxeter group has an associated graph called a Coxeter diagram, which describes the spatial relations between a collection of reflecting hyperplanes. There is a reflecting hyperplane [the  $r_i$  in Eq. (D1)] for each vertex of the diagram and the edges represent the dihedral angles between different reflecting hyperplanes [corresponding to the  $p_{ij}$  in Eq. (D1)]. Unmarked edges correspond to dihedral angles of  $\pi/3$ , whereas edges marked by  $p > 3$  correspond to dihedral angles of  $\pi/p$ . Vertices that are not connected by edges have dihedral angles of  $\pi/2$ . Figure 13 gives an example using the Coxeter diagram  $\bullet \xrightarrow{4} \bullet \xrightarrow{4} \bullet$ .

Given a Coxeter diagram, one can build uniform tilings using Wythoff's construction [81]. Consider the kaleidoscope corresponding to a given Coxeter diagram (for an example, see Fig. 13). We mark a subset of the vertices of a Coxeter diagram by ringing them. We then place a generating vertex inside the fundamental domain of the kaleidoscope, where the generating point is equidistant from all the reflecting hyperplanes that correspond to the ringed vertices. If a vertex is unringed, then the generating

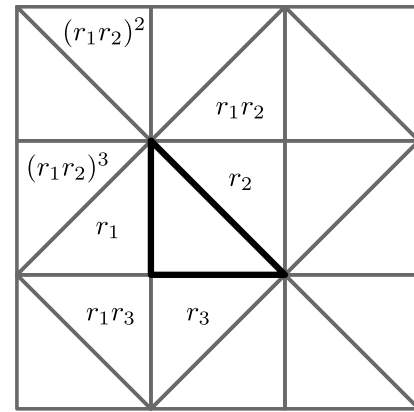


FIG. 13. An illustration of the Coxeter kaleidoscope. The vertices of the Coxeter diagram  $\bullet \xrightarrow{4} \bullet \xrightarrow{4} \bullet$  correspond to three reflecting hyperplanes  $r_1$ ,  $r_2$ , and  $r_3$  (labeled left to right). In the figure, the reflecting hyperplanes are the sides of the black triangle (the fundamental region). As specified by the diagram,  $r_1$  and  $r_3$  have dihedral angle  $\pi/2$ , whereas  $r_1$  and  $r_2$  have dihedral angle  $\pi/4$  (as do  $r_2$  and  $r_3$ ). We show a subset of the (infinite) reflections of the fundamental region and we label some of these reflections in terms of  $r_1$ ,  $r_2$ , and  $r_3$ . From the figure, we see that  $(r_1 r_3)^2 = 1$  and  $(r_1 r_2)^4 = 1$ , matching the Coxeter diagram.

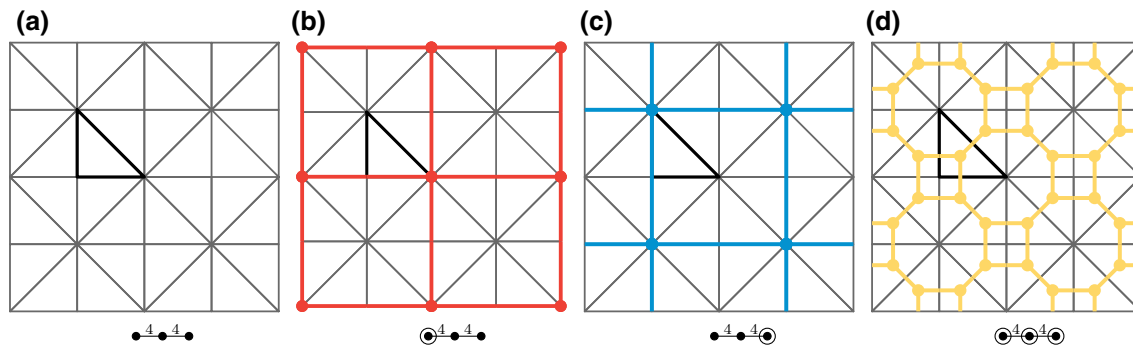


FIG. 14. Examples of Wythoff's construction applied to the Coxeter diagram  $\bullet^4\text{---}\bullet^4\text{---}\bullet$ . (a) The Coxeter kaleidoscope described in Fig. 13. The fundamental region is highlighted in black. (b) Ringing the first vertex of the Coxeter diagram corresponds to placing the generating point at one of the corners of the fundamental region (red circle). The resultant tessellation is a square tiling. (c) By symmetry, ringing the third vertex of the diagram also leads to a square tiling. (d) Ringing all three vertices of the Coxeter diagram corresponds to placing the generating vertex at the center of the fundamental region (equidistant from each reflecting hyperplane). In the resultant tessellation, two octahedra and one square meet at each vertex.

point lies on the corresponding reflecting hyperplane. The uniform tessellation is then the reflection of the generating point in all of the reflecting hyperplanes. Figure 14 shows some examples of Wythoff's construction applied to  $\bullet^4\text{---}\bullet^4\text{---}\bullet$ .

The useful thing about Coxeter diagrams in our context is that the kaleidoscope corresponding to a particular Coxeter diagram is exactly a  $d$ -colex, where  $d$  is the number of vertices of the diagram minus one. To see this, note that a Coxeter diagram naturally describes a simplicial complex. Furthermore, the complex will be  $(d + 1)$ -vertex colorable, as we can pick  $(d + 1)$  colors for the vertices of the fundamental region such that no two vertices have the same color, and the rest of the tessellation is formed by reflections of this fundamental region. In 2D, we have the following (affine) Coxeter diagrams:  $\bullet^4\text{---}\bullet^4\text{---}\bullet$ ,  $\triangle$ , and

$\bullet\text{---}\bullet^6\text{---}\bullet$ ; each of which describes an affine Coxeter group and hence an infinite 2-colex. Furthermore, in certain cases, different markups of a Coxeter diagram correspond to toric-code lattices that are related to the colex via morphing. As an example, consider again  $\bullet^4\text{---}\bullet^4\text{---}\bullet$ . As shown in Fig. 14,  $\odot^4\text{---}\bullet^4\text{---}\bullet$  and  $\bullet^4\text{---}\bullet^4\text{---}\odot$  correspond to square tilings. These are exactly the lattices we obtain if we morph the colorable 2-balls with associated 2-hyperoctahedron codes in the color-code lattice described by  $\bullet^4\text{---}\bullet^4\text{---}\bullet$ .

Let us consider another example, this time in 3D. In Fig. 15, we illustrate the tessellation correspond-

ing to the Coxeter diagram  $\bullet^4\text{---}\bullet^4\text{---}\bullet^4$ . This diagram gives a 3-colex, the dual of which is a uniform tessellation where one square, one truncated octahedron, and two truncated

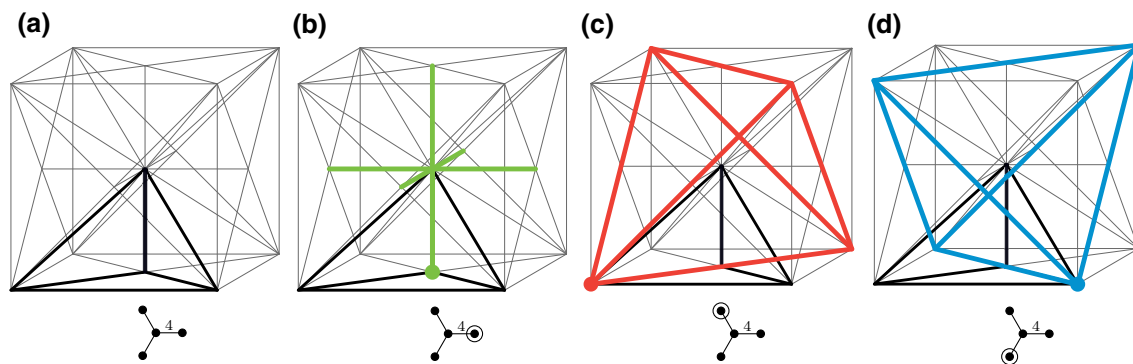


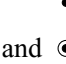



FIG. 15. Examples of Wythoff's construction applied to the Coxeter diagram  $\bullet^4\text{---}\bullet^4\text{---}\bullet^4$ . (a) The fundamental region is the tetrahedron highlighted in black. The reflecting hyperplanes are the four faces of the tetrahedron. (b) Applying Wythoff's construction with the markup  $\odot^4\text{---}\bullet^4\text{---}\bullet^4\text{---}\bullet^4$  produces the cubic honeycomb. (c) Applying Wythoff's construction with the markup  $\odot^4\text{---}\bullet^4\text{---}\bullet^4\text{---}\odot^4$  produces a uniform tessellation where eight tetrahedra and six octahedra meet at each vertex. This tessellation is sometimes called the tetrahedral-octahedral honeycomb. (d) The same tessellation as in (c) but rotated by  $\pi/2$ .

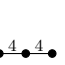
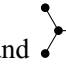



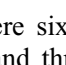
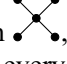
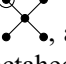


cuboctahedra meet at every vertex (a tessellation called the cantitruncated cubic honeycomb). In this case, the

markups , , and  give the cubic honeycomb and two tetrahedral-octahedral honeycombs (see Fig. 15). These are exactly the toric-code lattices that are produced by morphing the colorable 3-balls with associated 3-hyperoctahedron codes in the color-code lattice

described by . Furthermore, these are exactly the toric codes (with the appropriate boundary conditions) that have a transversal logical  $C_3$  gate [22].

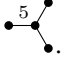
One may ask how general the Coxeter diagram approach illustrated in the previous two examples is. While the markups of Coxeter diagrams are generically related to restricted color-code lattices, the most elegant examples are color codes the structure of which is described by Cox-

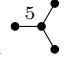
eter diagrams that are star graphs, e.g.,  and . The fundamental region of a Coxeter group corresponding to such a diagram is a right-angled simplex, i.e., a simplex where all facets except one meet at right angles at one vertex (see the fundamental regions in Figs. 13 and 15). In such cases, all the colorable  $d$ -balls of one color will have associated  $d$ -hyperoctahedron codes. Therefore, we can morph these colorable  $d$ -balls to obtain  $d$  toric codes with a transversal gate implemented by  $C_d$ .

In 4D, there is a single affine Coxeter diagram with the required star-graph structure: . This diagram describes a 4-colex dual to a tessellation where four truncated octaplexes and one tesseract meet at each vertex. An octaplex (or hyperdiamond) is a regular 4-polytope described by the ringed Coxeter diagram , where six octaplexes meet at each vertex of the polytope and three meet at each edge. From , we can construct , a regular tessellation where every cell is a 4-hyperoctahedron and three 4-cells meet at each face. Morphing the colorable 4-balls with associated 4-hyperoctahedron codes in  produces four toric codes defined on  tessellations with a transversal gate implemented by  $C_4$ . With appropriate

boundary conditions, these are the 4D toric codes with a transversal logical  $C_4$  gate detailed in Ref. [23].


There are no further affine Coxeter diagrams in higher-dimensional Euclidean space with the required star-graph structure. However, Coxeter groups also describe tessellations in hyperbolic space and there are hyperbolic Coxeter groups with star-graph Coxeter diagrams in 2D and 3D [86,87]. In 3D hyperbolic space, we have the Coxeter dia-

gram . The color code defined on this 3-colex has stabilizer weights of 120, 24, 10, 8, 6, and 4. Wythoff's construction gives us the tessellations detailed in Table I. We expect that morphing the colorable 3-balls with asso-

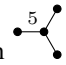
ciated 3-hyperoctahedron codes in  would give toric codes with a transversal gate implemented by  $C_3$  gates. As hyperbolic toric codes are finite rate, this may be an interesting set of codes to explore.

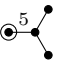

## APPENDIX E: MORPHING THE “BNB” LATTICE

Here, we briefly discuss an example of a 3D HCT code that contains both color-code and toric-code regions. To construct the code we apply our morphing procedure to the lattice described in Ref. [88] (which we call the “BNB lattice” after the authors). The BNB lattice contains colorable 3-balls with associated 3-hyperoctahedron codes but they are not all the same color (in fact, they are split evenly between the four colors) and they do not cover all the qubits in the code. Suppose that we start with a color code defined on a BNB lattice that tessellates a closed manifold. One can verify that when we morph the 3-hyperoctahedron codes, we obtain a tetrahedral-octahedral honeycomb (with a slight modification; see Fig. 16). In the tetrahedral-octahedral honeycomb, six tetrahedra and eight tetrahedra meet at each vertex. It can be constructed using

Wythoff's construction with the Coxeter diagram  (see Appendix D).

The HCT code defined on the morphed BNB lattice has a particularly simple implementation of a non-Clifford gate. Namely, we apply  $R_3$  and  $R_3^\dagger$  to the simplex qubits (following the qubit bipartition of the parent color code)

TABLE I. Some of the tessellations that can be constructed from the Coxeter diagram  using Wythoff's construction. Toric codes defined on these tessellations have the stabilizer weights shown in the fourth column.

Wythoff construction	Name	Structure	Stabilizer weights
	Order-4 dodecahedral	8 dodecahedra at each vertex	5 and 6
	Alternated order-5 cubic	20 tetrahedra and 12 icosahedra at each vertex	3 and 30



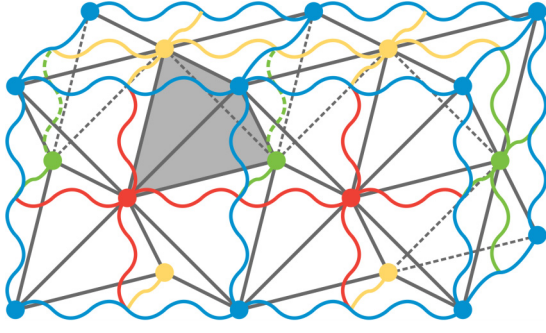


FIG. 16. A portion of the morphed BNB lattice. The gray edges show the underlying tetrahedral-octahedral lattice. We have one qubit for each edge linking vertices of the same color and one qubit for each tetrahedron (one of which we shade in gray).  $X$ -type stabilizer generators are associated with vertices and  $Z$ -type stabilizer generators are associated with edges linking vertices of different colors.

and  $C_3$  to the triple of edge qubits at each octahedron. If we choose a lattice with tetrahedral boundary conditions (as in Ref. [88]), this gate will implement a logical  $R_3$  gate.

## APPENDIX F: MORPHING STELLATED COLOR CODES

In this appendix, we apply our morphing procedure to stellated color codes [89]. We focus on distance-3 stellated color codes based on the 4.8.8 tessellation, though we expect that our results will generalize to the entire code family. Following Ref. [89], we parametrize the codes by an integer  $s \geq 3$ , the order of the rotational symmetry of the code. The codes in the subfamily that we consider have parameters  $[[5s, s, 3]]$ . We explain the construction of distance-3 stellated color codes via examples in Fig. 17. We note that when  $s$  is odd, the stellated codes contain twist defects [89,90].

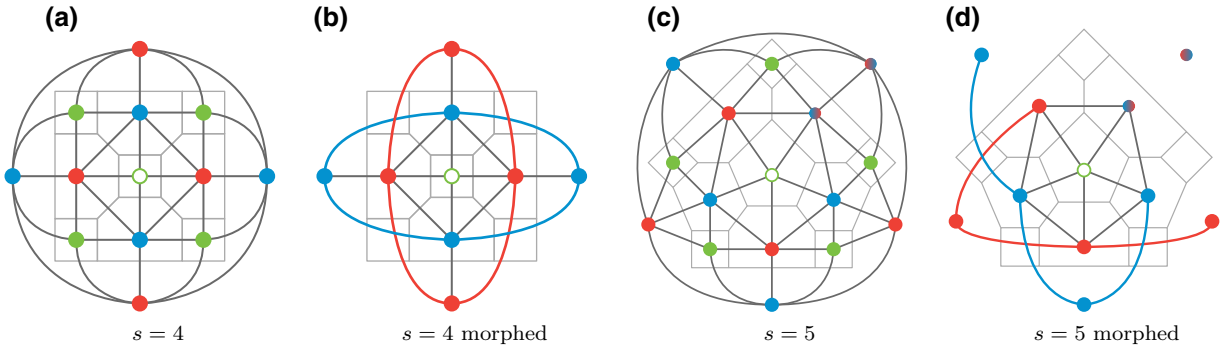


FIG. 17. Morphing stellated color codes. We show the (a)  $s = 4$  and (c)  $s = 5$  distance-3 stellated color codes, which have parameters  $[[20,4,3]]$  and  $[[25,5,3]]$ , respectively. We show the primal lattice in light gray for ease of comparison with Ref. [89]. (b),(d) The corresponding morphed codes, with parameters  $[[12,4,2]]$  and  $[[15,5,2]]$ . We note that the central vertex has no associated stabilizer, which we indicate by making it hollow. For odd  $s$ , the color-code colorability condition is unsatisfied, indicating the presence of a twist defect. We represent this pictorially by blended  $r/b$  vertices and edges.

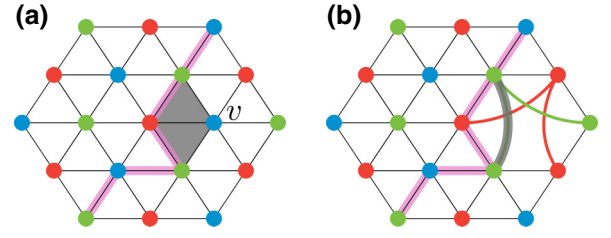


FIG. 18. The local-lift subroutine of our HCT-code decoder. (a) We show part of a 2-colex, with a matching (subset of edges) highlighted in pink. If we apply local lift at the central  $r$  vertex, we obtain the highlighted gray faces. These faces have the required property that their boundary equals the matching, when restricted to the neighborhood of  $v$ . (b) The application of local lift for the same matching but now in a HCT-code lattice. For the ball code defined on  $\mathcal{B}^v$ , the  $Z$  operator with support equal to the highlighted faces in (a) is the logical operator acting on the edge qubit highlighted in gray in (b). Therefore, for this matching, local lift returns the highlighted edge when it is applied at the central  $r$  vertex.

We now apply our morphing procedure to distance-3 stellated color codes. We morph all colorable 2-balls with associated  $[[4,2,2]]$  codes, giving a family of stellated HCT codes with parameters  $[[3s, s, 2]]$ . These codes have a high encoding rate and inherit the transversal gates of the stellated color codes. In particular, for even  $s$ , the stellated color codes have a logical  $S^{\otimes s} = \tilde{S}$ . In the morphed stellated color codes, the logical  $S^{\otimes s}$  gate is implemented by  $S$  and  $S^\dagger$  on the color-code qubits (as before) and by  $C_2$  gates on the pairs of toric-code qubits arising from each  $[[4,2,2]]$  code.

One interesting avenue to explore is the generalization of these results to higher dimensions. It seems plausible that stellated color codes could exist in 3D and we expect that these codes would have fault-tolerant logical  $R_3$  gates.

## APPENDIX G: HCT-CODE DECODER DETAILS

In this appendix, we explain the local-lift step of our 2D HCT-code decoder and we comment on the overall time complexity of our decoder.

Let  $\mathcal{L}$  be a 2-colex and let  $\tilde{\mathcal{L}}$  be a HCT-code lattice produced from  $\mathcal{L}$  by morphing a subset of the colorable 2-balls of  $\mathcal{L}$ . Also, let  $\mu \subseteq \tilde{\mathcal{L}}_1$  be the matching produced in the second step of our decoding algorithm (see Sec. V A). We use  $\mu|_v = \{e \in \mu : v \subseteq e\}$  to denote the restriction of  $\mu$  to the neighborhood of a vertex  $v$ . In the color-code regions of  $\tilde{\mathcal{L}}$ , for each  $r$  vertex  $v$  in the matching, local lift returns a set of faces  $\varphi \subseteq \mathcal{L}_2 \cap \text{St}_2(v)$ , such that  $(\partial_{2,1}\varphi)|_v = \mu|_v$ . In the toric-code regions of  $\tilde{\mathcal{L}}$ , we first work out which faces local lift would return if it were to be applied in  $\mathcal{L}$  with the same matching. For a given  $r$  vertex  $v$  on the boundary of a morphed colorable 2-ball, this set of faces will be

TABLE II. The distillation costs for various MSD protocols to achieve target error rates  $p_{\text{targ}}$ , assuming an input error rate of  $p = 0.01$ . The MEK+ protocol ( $C_{\text{MEK+}}$ ) equals or betters the original MEK protocol [17] ( $C_{\text{MEK}}$ ) and betters the tri-orthogonal protocol [32] ( $C_{\Delta}$ ) for  $p_{\text{targ}} \in \{10^{-6}, 10^{-9}, 10^{-10}\}$ . The “Sequence” column shows the sequence of distillation protocols used in the MEK+ protocol, where 5 is 10-to-2, 10 is 10-to-1, and 15 is 15-to-1;  $p_{\text{actual}}$  is the output error rate achieved by the sequence.

$-\log_{10} p_{\text{targ}}$	$C_{\Delta}$	$C_{\text{MEK}}$	$C_{\text{MEK+}}$	Sequence	$-\log_{10} p_{\text{actual}}$
3	5.521	5.521	5.521	5	3.030
4	17.44	17.44	17.44	15	4.443
5	27.86	27.86	27.86	5-5	5.104
6	56.07	83.99	43.39	10-5	6.969
7	58.30	83.99	69.41	10-10	7.923
8	89.26	139.3	130.2	10-15	10.32
9	139.3	139.3	130.2	10-15	10.32
10	179.4	261.7	130.2	10-15	10.32
11	179.4	261.7	217.0	10-5-5	12.98
12	187.9	418.0	217.0	10-5-5	12.98
13	225.6	418.0	347.1	10-10-5	14.89
14	285.6	419.9	347.1	10-10-5	14.89
15	315.5	696.7	555.3	10-10-10	15.85
16	406.2	696.7	650.9	10-5-15	19.36
17	529.5	696.7	650.9	10-5-15	19.36
18	574.1	1260	650.9	10-5-15	19.36
19	574.1	1260	650.9	10-5-15	19.36
20	574.1	1260	1041	10-10-15	22.22
21	575.9	1260	1041	10-10-15	22.22
22	604.3	1308	1041	10-10-15	22.22
23	652.3	2090	1085	10-5-5-5	25.01
24	731.5	2090	1085	10-5-5-5	25.01
25	853.1	2090	1085	10-5-5-5	25.01
26	914.0	2090	1735	10-10-5-5	28.83
27	947.5	2100	1735	10-10-5-5	28.83
28	1015	2181	1735	10-10-5-5	28.83
29	1125	3483	1954	10-15-15	29.48
30	1301	3483	2776	10-10-10-5	30.74

equal to the support of a logical  $Z$  operator of the ball code. Local lift then simply returns the edge qubits acted on by this logical operator. Figure 18 shows an example.

We claim that our decoder has time complexity  $O(N^3)$ , where  $N$  is the number of physical qubits in the code. First, we note that there are  $O(N)$  vertices and  $O(N)$  edges in the 2D HCT-code lattice. In the first step of the decoder, we call MWPM twice, giving a time complexity of  $O(N^3)$  due to the BLOSSOM algorithm. In the second step of the decoder, we iterate through the edges in the matching, where (in the worst case) there will be  $O(N)$  such edges. For each edge  $e$ , the local-modification step only requires simple calculations in the neighbourhood of  $e$ , which is of constant size by assumption. Therefore each local modification takes constant time and this the second step has time complexity  $O(N)$ . The third step of the decoder is similar: we iterate through (at most)  $O(N)$  vertices and  $O(N)$  edges, applying a constant time local lift at each vertex. Hence the third step also has time complexity  $O(N)$ , implying that the overall time complexity is  $O(N^3)$ .

## APPENDIX H: COMPARING DISTILLATION COSTS

We evaluate the utility of our 10-to-1 MSD protocol by comparing the required distillation cost  $C$  to achieve a certain target error rate  $p_{\text{targ}}$ , assuming an input error rate of  $p = 0.01$ , for three multiround MSD protocols (see Table II). The MEK protocol [17] uses 15-to-1 and 10-to-1 distillation and the triorthogonal protocol [32] uses triorthogonal codes. In the MEK+ protocol, we augment the MEK protocol with 10-to-1 distillation.

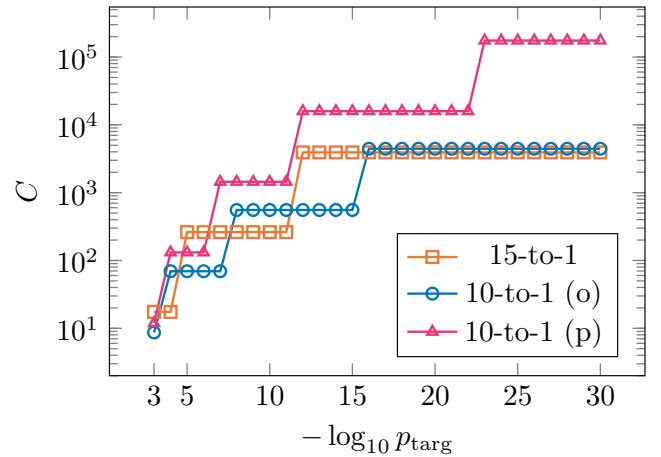


FIG. 19. A plot showing the distillation cost  $C$  for different target error rates  $p_{\text{targ}}$ , assuming an input error rate of  $p = 0.01$ . For certain values of  $p_{\text{targ}}$ , we find that the cost of our 10-to-1 protocol is lower than the cost of the 15-to-1 protocol, where “(o)” and “(p)” refer to the optimistic and pessimistic noise models for CCZ states described in Sec. III B, respectively.

We can also directly compare the distillation cost of the 10-to-1 protocol against the 15-to-1 protocol (see Fig. 19). Assuming the optimistic noise model for  $CCZ$  states described in Sec. III B, we find that the 10-to-1 protocol has a lower cost than the 15-to-1 protocol for target error rates  $p_{\text{targ}} \in \{10^{-3}, 10^{-5}, 10^{-6}, 10^{-7}, 10^{-12}, 10^{-13}, 10^{-14}, 10^{-15}\}$ . Furthermore, assuming the pessimistic noise model for  $CCZ$  states, we find that the 10-to-1 protocol has a lower cost than the 15-to-1 protocol for target error rates  $p_{\text{targ}} \in \{10^{-3}, 10^{-5}, 10^{-6}\}$ .

- 
- [1] D. Aharonov and M. Ben-Or, Fault-tolerant quantum computation with constant error rate, *SIAM J. Comput.* **38**, 1207 (2008).
  - [2] E. Knill, R. Laflamme, and W. H. Zurek, Resilient quantum computation, *Science* **279**, 342 (1998).
  - [3] A. Y. Kitaev, Quantum computations: Algorithms and error correction, *Russ. Math. Surv.* **52**, 1191 (1997).
  - [4] D. Gottesman, Fault-tolerant quantum computation with constant overhead, *Quantum Inf. Comput.* **14**, 1338 (2014).
  - [5] O. Fawzi, A. Grospellier, and A. Leverrier, in *2018 IEEE 59th Annual Symposium on Foundations of Computer Science (FOCS)* (IEEE, Paris, 2018), p. 743.
  - [6] D. Litinski, A game of surface codes: Large-scale quantum computing with lattice surgery, *Quantum* **3**, 128 (2019).
  - [7] A. G. Fowler and C. Gidney, Low overhead quantum computation using lattice surgery, arXiv preprint [arXiv:1808.06709](https://arxiv.org/abs/1808.06709) (2019).
  - [8] C. Chamberland, K. Noh, P. Arrangoiz-Arriola, E. T. Campbell, C. T. Hann, J. Iverson, H. Putterman, T. C. Bohdanowicz, S. T. Flammia, A. Keller, G. Refael, J. Preskill, L. Jiang, A. H. Safavi-Naeini, O. Painter, and F. G. S. L. Brandão, Building a fault-tolerant quantum computer using concatenated cat codes, arXiv preprint [arXiv:2012.04108](https://arxiv.org/abs/2012.04108) (2020).
  - [9] I. H. Kim, E. Lee, Y.-H. Liu, S. Pallister, W. Pol, and S. Roberts, Fault-tolerant resource estimate for quantum chemical simulations: Case study on Li-ion battery electrolyte molecules, arXiv preprint [arXiv:2104.10653](https://arxiv.org/abs/2104.10653) (2021).
  - [10] M. E. Beverland, A. Kubica, and K. M. Svore, Cost of Universality: A Comparative Study of the Overhead of State Distillation and Code Switching with Color Codes, *PRX Quantum* **2**, 020341 (2021).
  - [11] L. Egan, D. M. Debroy, C. Noel, A. Risinger, D. Zhu, D. Biswas, M. Newman, M. Li, K. R. Brown, M. Cetina, and C. Monroe, Fault-tolerant operation of a quantum error-correction code, arXiv preprint [arXiv:2009.11482](https://arxiv.org/abs/2009.11482) (2021).
  - [12] C. K. Andersen, A. Remm, S. Lazar, S. Krinner, N. Lacroix, G. J. Norris, M. Gabureac, C. Eichler, and A. Wallraff, Repeated quantum error detection in a surface code, *Nat. Phys.* **16**, 875 (2020).
  - [13] Z. Chen *et al.*, Exponential suppression of bit or phase errors with cyclic error correction, *Nature* **595**, 383 (2021).
  - [14] E. H. Chen, T. J. Yoder, Y. Kim, N. Sundaresan, S. Srinivasan, M. Li, A. D. Córcoles, A. W. Cross, and M. Takita, Calibrated decoders for experimental quantum error correction, arXiv preprint [arXiv:2110.04285](https://arxiv.org/abs/2110.04285) (2021).
  - [15] A. Erhard, H. Poulsen Nautrup, M. Meth, L. Postler, R. Stricker, M. Stadler, V. Negnevitsky, M. Ringbauer, P. Schindler, H. J. Briegel, R. Blatt, N. Friis, and T. Monz, Entangling logical qubits with lattice surgery, *Nature* **589**, 220 (2021).
  - [16] S. Bravyi and A. Kitaev, Universal quantum computation with ideal Clifford gates and noisy ancillas, *Phys. Rev. A* **71**, 022316 (2005).
  - [17] A. M. Meier, B. Eastin, and E. Knill, Magic-state distillation with the four-qubit code, *Quantum Inf. Comput.* **13**, 195 (2013).
  - [18] H. Bombin and M. A. Martin-Delgado, Topological Quantum Distillation, *Phys. Rev. Lett.* **97**, 180501 (2006).
  - [19] H. Bombin and M. A. Martin-Delgado, Topological Computation without Braiding, *Phys. Rev. Lett.* **98**, 160502 (2007).
  - [20] A. M. Kubica, Ph.D. thesis, Caltech, 2018.
  - [21] A. Kubica, B. Yoshida, and F. Pastawski, Unfolding the color code, *New J. Phys.* **17**, 083026 (2015).
  - [22] M. Vasmer and D. E. Browne, Three-dimensional surface codes: Transversal gates and fault-tolerant architectures, *Phys. Rev. A* **100**, 012312 (2019).
  - [23] T. Jochym-O'Connor and T. J. Yoder, A four-dimensional toric code with non-Clifford transversal gates, *Phys. Rev. Res.* **3**, 013118 (2021).
  - [24] E. Dennis, A. Kitaev, A. Landahl, and J. Preskill, Topological quantum memory, *J. Math. Phys.* **43**, 4452 (2002).
  - [25] A. G. Fowler, Minimum weight perfect matching of fault-tolerant topological quantum error correction in average  $O(1)$  parallel time, *Quantum Inf. Comput.* **15**, 145 (2015).
  - [26] A. Kubica and N. Delfosse, Efficient color code decoders in  $\$d/\text{geq } 2\$$  dimensions from toric code decoders, arXiv preprint [arXiv:1905.07393](https://arxiv.org/abs/1905.07393) (2019).
  - [27] D. Gottesman, Stabilizer codes and quantum error correction, arXiv preprint [arXiv:quant-ph/9705052](https://arxiv.org/abs/quant-ph/9705052) (1997).
  - [28] We observe that morphing is similar to the disentangling step of entanglement renormalization [91].
  - [29] A. M. Steane, Multiple-particle interference and quantum error correction, *Proc. R. Soc. London. Series A: Math. Phys. Eng. Sci.* **452**, 2551 (1996).
  - [30] E. Knill, Quantum computing with realistically noisy devices, *Nature* **434**, 39 (2005).
  - [31] E. Knill, Fault-tolerant postselected quantum computation: Schemes, arXiv preprint [arXiv:quant-ph/0402171](https://arxiv.org/abs/quant-ph/0402171) (2004).
  - [32] S. Bravyi and J. Haah, Magic-state distillation with low overhead, *Phys. Rev. A* **86**, 052329 (2012).
  - [33] E. T. Campbell and M. Howard, Unifying Gate Synthesis and Magic State Distillation, *Phys. Rev. Lett.* **118**, 060501 (2017).
  - [34] M. B. Hastings and J. Haah, Distillation with Sublogarithmic Overhead, *Phys. Rev. Lett.* **120**, 050504 (2018).
  - [35] J. Haah, M. B. Hastings, D. Poulin, and D. Wecker, Magic state distillation at intermediate size, *Quantum Inf. Comput.* **18**, 0114 (2018).
  - [36] J. Haah and M. B. Hastings, Codes and protocols for distilling  $\$T\$$ , controlled- $\$SS\$$ , and Toffoli gates, *Quantum* **2**, 71 (2018).
  - [37] A. Steane, Quantum Reed-Muller codes, *IEEE Trans. Inf. Theory* **45**, 1701 (1999).

- [38] J. T. Anderson, G. Duclos-Cianci, and D. Poulin, Fault-Tolerant Conversion between the Steane and Reed-Muller Quantum Codes, *Phys. Rev. Lett.* **113**, 080501 (2014).
- [39] F. J. MacWilliams and N. J. A. Sloane, *The Theory of Error Correcting Codes*, North-Holland Mathematical Library (North-Holland Pub. Co., Amsterdam, 1977), Vol. 16.
- [40] E. T. Campbell, The smallest interesting colour code, <https://earlrcampbell.com/2016/09/26/the-smallest-interesting-colour-code/> (2016), (accessed: 2021-07-20).
- [41] A. Paetznick and B. W. Reichardt, Universal Fault-Tolerant Quantum Computation with Only Transversal Gates and Error Correction, *Phys. Rev. Lett.* **111**, 090505 (2013).
- [42] C. Jones, Low-overhead constructions for the fault-tolerant Toffoli gate, *Phys. Rev. A* **87**, 022328 (2013).
- [43] D. Litinski, Magic state distillation: Not as costly as you think, *Quantum* **3**, 205 (2019).
- [44] C. Gidney and A. G. Fowler, Efficient magic state factories with a catalyzed  $—CCZ>$  to  $2—T>$  transformation, *Quantum* **3**, 135 (2019).
- [45] E. T. Campbell and M. Howard, Unified framework for magic state distillation and multiqubit gate synthesis with reduced resource cost, *Phys. Rev. A* **95**, 022316 (2017).
- [46] H. Bombín, Gauge color codes: Optimal transversal gates and gauge fixing in topological stabilizer codes, *New J. Phys.* **17**, 083002 (2015).
- [47] A. Kubica and M. E. Beverland, Universal transversal gates with color codes—a simplified approach, *Phys. Rev. A* **91**, 032330 (2015).
- [48] F. H. E. Watson, E. T. Campbell, H. Anwar, and D. E. Browne, Qudit color codes and gauge color codes in all spatial dimensions, *Phys. Rev. A* **92**, 022312 (2015).
- [49] H. Bombín, Transversal gates and error propagation in 3D topological codes, arXiv preprint [arXiv:1810.09575](https://arxiv.org/abs/1810.09575) (2018).
- [50] B. Criger and B. Terhal, Noise thresholds for the  $[[4, 2, 2]]$ -concatenated toric code, *Quantum Inf. Comput.* **16**, 1261 (2016).
- [51] H. Bombín, G. Duclos-Cianci, and D. Poulin, Universal topological phase of two-dimensional stabilizer codes, *New J. Phys.* **14**, 073048 (2012).
- [52] N. Delfosse, Decoding color codes by projection onto surface codes, *Phys. Rev. A* **89**, 012317 (2014).
- [53] V. Kolmogorov, BLOSSOM V: A new implementation of a minimum cost perfect matching algorithm, *Math. Program. Comput.* **1**, 43 (2009).
- [54] <https://github.com/MikeVasmer/hybrid-decoder>.
- [55] N. Delfosse and N. H. Nickerson, Almost-linear time decoding algorithm for topological codes, arXiv preprint [arXiv:1709.06218](https://arxiv.org/abs/1709.06218) (2017).
- [56] B. J. Brown and D. J. Williamson, Parallelized quantum error correction with fracton topological codes, *Phys. Rev. Res.* **2**, 013303 (2020).
- [57] J. P. Bonilla Ataides, D. K. Tuckett, S. D. Bartlett, S. T. Flammia, and B. J. Brown, The XZZX surface code, *Nat. Commun.* **12**, 2172 (2021).
- [58] H. Poulsen Nautrup, N. Friis, and H. J. Briegel, Fault-tolerant interface between quantum memories and quantum processors, *Nat. Commun.* **8**, 1321 (2017).
- [59] N. Shutty and C. Chamberland, Finding fault-tolerant Clifford circuits using satisfiability modulo theories solvers and decoding merged color-surface codes, arXiv preprint [arXiv:2201.12450](https://arxiv.org/abs/2201.12450) (2022).
- [60] C. Chamberland, A. Kubica, T. J. Yoder, and G. Zhu, Triangular color codes on trivalent graphs with flag qubits, *New J. Phys.* **22**, 023019 (2020).
- [61] J. Harrington, Ph.D. thesis, Caltech, 2004.
- [62] C. Wang, J. Harrington, and J. Preskill, Confinement-Higgs transition in a disordered gauge theory and the accuracy threshold for quantum memory, *Ann. Phys. (NY)* **303**, 31 (2003).
- [63] J. K. Iverson, Ph.D. thesis, Caltech, 2020.
- [64] J. Iverson and A. Kubica, (to be published, 2022).
- [65] R. Raussendorf and J. Harrington, Fault-Tolerant Quantum Computation with High Threshold in Two Dimensions, *Phys. Rev. Lett.* **98**, 190504 (2007).
- [66] D. S. Wang, A. G. Fowler, A. M. Stephens, and L. C. L. Hollenberg, Threshold error rates for the toric and planar codes, *Quantum Inf. Comput.* **10**, 456 (2010).
- [67] S. Bravyi, M. Suchara, and A. Vargo, Efficient algorithms for maximum likelihood decoding in the surface code, *Phys. Rev. A* **90**, 032326 (2014).
- [68] C. T. Chubb, General tensor network decoding of 2D Pauli codes, arXiv preprint [arXiv:2101.04125](https://arxiv.org/abs/2101.04125) (2021).
- [69] H. G. Katzgraber, H. Bombín, and M. A. Martin-Delgado, Error Threshold for Color Codes and Random Three-Body Ising Models, *Phys. Rev. Lett.* **103**, 090501 (2009).
- [70] A. Honecker, M. Picco, and P. Pujol, Universality Class of the Nishimori Point in the 2D  $\pm J$  Random-Bond Ising Model, *Phys. Rev. Lett.* **87**, 047201 (2001).
- [71] F. Merz and J. T. Chalker, Two-dimensional random-bond Ising model, free fermions, and the network model, *Phys. Rev. B* **65**, 054425 (2002).
- [72] M. Ohzeki, Locations of multicritical points for spin glasses on regular lattices, *Phys. Rev. E* **79**, 021129 (2009).
- [73] D. Poulin, Stabilizer Formalism for Operator Quantum Error Correction, *Phys. Rev. Lett.* **95**, 230504 (2005).
- [74] A. Kubica and M. Vasmer, Single-shot quantum error correction with the three-dimensional subsystem toric code, arXiv preprint [arXiv:2106.02621](https://arxiv.org/abs/2106.02621) (2021).
- [75] C. Vuillot and N. P. Breuckmann, Quantum pin codes, arXiv preprint [arXiv:1906.11394](https://arxiv.org/abs/1906.11394) (2019).
- [76] H. Bombín and M. A. Martin-Delgado, Exact topological quantum order in  $D = 3$  and beyond: Branyons and brane-net condensates, *Phys. Rev. B* **75**, 075103 (2007).
- [77] A. Y. Kitaev, in *Quantum Communication, Computing, and Measurement*, edited by O. Hirota, A. S. Holevo, and C. M. Caves (Springer US, Boston, MA, 1997), p. 181.
- [78] A. Y. Kitaev, Fault-tolerant quantum computation by anyons, *Ann. Phys. (NY)* **303**, 2 (2003).
- [79] A. R. Calderbank and P. W. Shor, Good quantum error-correcting codes exist, *Phys. Rev. A* **54**, 1098 (1996).
- [80] A. Krishna and J.-P. Tillich, Towards Low Overhead Magic State Distillation, *Phys. Rev. Lett.* **123**, 070507 (2019).
- [81] H. S. M. Coxeter, *Regular Polytopes* (Dover, New York, 1973).
- [82] M. Vasmer, Ph.D. thesis, Department of Physics and Astronomy, University College London, 2019.
- [83] N. P. Breuckmann and B. M. Terhal, Constructions and noise threshold of hyperbolic surface codes, *IEEE Trans. Inf. Theory* **62**, 3731 (2016).



- [84] N. P. Breuckmann, C. Vuillot, E. Campbell, A. Krishna, and B. M. Terhal, Hyperbolic and semi-hyperbolic surface codes for quantum storage, [Quantum Sci. Technol. 2, 035007 \(2017\)](#).
- [85] N. P. Breuckmann, Ph.D. thesis, Fakultät für Mathematik, Informatik und Naturwissenschaften, RWTH Aachen University (2018).
- [86] J. E. Humphreys, *Reflection Groups and Coxeter Groups* (Cambridge University Press, 1990), 1st ed.
- [87] M. Davis, *The Geometry and Topology of Coxeter Groups*, London Mathematical Society Monographs Series (Princeton University Press, Princeton, Cambridge, 2008).
- [88] B. J. Brown, N. H. Nickerson, and D. E. Browne, Fault-tolerant error correction with the gauge color code, [Nat. Commun. 7, 12302 \(2016\)](#).
- [89] M. S. Kesselring, F. Pastawski, J. Eisert, and B. J. Brown, The boundaries and twist defects of the color code and their applications to topological quantum computation, [Quantum 2, 101 \(2018\)](#).
- [90] H. Bombín, Topological Order with a Twist: Ising Anyons from an Abelian Model, [Phys. Rev. Lett. 105, 030403 \(2010\)](#).
- [91] G. Vidal, Entanglement Renormalization, [Phys. Rev. Lett. 99, 220405 \(2007\)](#).